Ore Geology Reviews 91 (2017) 110–132

Contents lists available at ScienceDirect

Ore Geology Reviews

journal homepage: www.elsevier.com/locate/oregeorev

Geology and ore genesis of the late Paleozoic Heijianshan Fe oxide–Cu (–Au) deposit in the Eastern Tianshan, NW China

Liandang Zhao[a,b], Huayong Chen[a,c,*], Li Zhang[a], Xiaoping Xia[d], Weifeng Zhang[e], Dengfeng Li[f], Wanjian Lu[a,b], Pei Liang[a,b], Rucao Li[a], Juntao Yang[g], Xuelu Yan[g]

[a] Key Laboratory of Mineralogy and Metallogeny, Guangzhou Institute of Geochemistry, Chinese Academy of Sciences, Guangzhou 510640, China
[b] University of Chinese Academy of Sciences, Beijing 100049, China
[c] State Key Laboratory of Geological Processes and Mineral Resources, China University of Geosciences, Wuhan 430074, China
[d] State Key Laboratory of Isotope Geochemistry, Chinese Academy of Sciences, Guangzhou 510640, China
[e] Wuhan Institute of Geology and Mineral Resources, China Geological Survey, Wuhan 434205, China
[f] School of Marine Sciences, Sun Yat-sen University, Guangzhou 510006, China
[g] No. 1 Geological Party of Xinjiang Bureau of Geology and Mineral Exploration, Changji, 831100, China

ARTICLE INFO

Keywords:
Paragenesis
Fluid inclusions
In-situ sulfur isotope
IOCG deposit
Eastern Tianshan
NW China

ABSTRACT

The Heijianshan Fe–Cu (–Au) deposit, located in the Aqishan-Yamansu belt of the Eastern Tianshan (NW China), is hosted in the mafic–intermediate volcanic and mafic–felsic volcaniclastic rocks of the Upper Carboniferous Matoutan Formation. Based on the pervasive alteration, mineral assemblages and crosscutting relationships of veins, six magmatic–hydrothermal stages have been established, including epidote alteration (Stage I), magnetite mineralization (Stage II), pyrite alteration (Stage III), Cu (–Au) mineralization (Stage IV), late veins (Stage V) and supergene alteration (Stage VI). The Stage I epidote–calcite–tourmaline–sericite alteration assemblage indicates a pre-mineralization Ca–Mg alteration event. Stage II Fe and Stage IV Cu (–Au) mineralization stages at Heijianshan can be clearly distinguished from alteration, mineral assemblages, and nature and sources of ore-forming fluids.

Homogenization temperatures of primary fluid inclusions in quartz and calcite from Stage I (189–370 °C), II (301–536 °C), III (119–262 °C) and V (46–198 °C) suggest that fluid incursion and mixing probably occurred during Stage I to II and Stage V, respectively. The Stage II magmatic–hydrothermal-derived Fe mineralization fluids were characterized by high temperature (> 300 °C), medium–high salinity (21.2–56.0 wt% NaCl equiv.) and being Na–Ca–Mg–Fe-dominated. These fluids were overprinted by the external low temperature (< 300 °C), medium–high salinity (19.0–34.7 wt% NaCl equiv.) and Ca–Mg-dominated basinal brines that were responsible for the subsequent pyrite alteration and Cu (–Au) mineralization, as supported by quartz CL images and H–O isotopes. Furthermore, *in-situ* sulfur isotopes also indicate that the sulfur sources vary in different stages, *viz.*, Stage II (magmatic–hydrothermal), III (basinal brine-related) and IV (magmatic–hydrothermal). Stage II disseminated pyrite has $\delta^{34}S_{fluid}$ values of 1.7–4.3‰, comparable with sulfur from magmatic reservoirs. $\delta^{34}S_{fluid}$ values (24.3–29.3‰) of Stage III Type A pyrite (coexists with hematite) probably indicate external basinal brine involvement, consistent with the analytical results of fluid inclusions. With the basinal brines further interacting with volcanic/volcaniclastic rocks of the Carboniferous Matoutan Formation, Stage III Type B pyrite–chalcopyrite–pyrrhotite assemblage (with low $\delta^{34}S_{fluid}$ values of 4.6–10.0‰) may have formed at low fO_2 and temperature (119–262 °C). The continuous basinal brine–volcanic/volcaniclastic rock interactions during the basin inversion (~325–300 Ma) may have leached sulfur and copper from the rocks, yielding magmatic-like $\delta^{34}S_{fluid}$ values (1.5–4.1‰). Such fluids may have altered pyrite and precipitated chalcopyrite with minor Au in Stage IV. Eventually, the Stage V low temperature (~160 °C) and low salinity meteoric water may have percolated into the ore-forming fluid system and formed late-hydrothermal veins.

The similar alteration and mineralization paragenetic sequences, ore-forming fluid sources and evolution, and tectonic settings of the Heijianshan deposit to the Mesozoic Central Andean IOCG deposits indicate that the former is probably the first identified Paleozoic IOCG-like deposit in the Central Asian Orogenic Belt.

* Corresponding author at: Guangzhou Institute of Geochemistry, Chinese Academy of Sciences, P.O. Box 1131, Tianhe District, Guangdong PRC, Guangzhou 510640, China.
E-mail address: huayongchen@gig.ac.cn (H. Chen).

http://dx.doi.org/10.1016/j.oregeorev.2017.10.014
Received 30 July 2017; Received in revised form 6 October 2017; Accepted 15 October 2017
Available online 16 October 2017

1. Introduction

The Eastern Tianshan of the Central Asian Orogenic Belt (CAOB; Fig. 1a and b) has been an important mineral exploration target in NW China due to the many important Fe (–Cu) deposits discovered, including Hongyuntan, Bailingshan, Heijianshan, Yamansu, Heifengshan, Shuangfengshan and Shaquanzi (Fig. 1c; Jiang et al., 2002; Cheng et al., 2008; Huang et al., 2013b). Of these Fe (–Cu) deposits, previous studies had predominantly focused on the petrology of the related intrusions (Li et al., 2011; Lei et al., 2013; Xu et al., 2014; Zhang et al., 2014) and the ore deposit geology (Mao et al., 2005; Qin et al., 2005; Han et al., 2014), but their ore genesis are still controversial. For example, the Hongyuntan Fe deposit has been classified as a hydrothermal metasomatic (Z.J. Zhang et al., 2012) or skarn (Zhang et al., 2013) deposit. The Bailingshan Fe deposit has been attributed to be a submarine volcanic-hosted (Li and Li, 1999; Xu et al., 2011), skarn (Mao et al., 2005) or hydrothermal metasomatic (W.F. Zhang et al., 2014) deposit. For the Yamansu Fe deposit, it has been proposed as a submarine volcanic-hosted (Hou et al., 2014; Li et al., 2014) or skarn (Mao et al., 2005; Zeng et al., 2014) deposit. Furthermore, Huang et al. (2013c) argued that Shaquanzi, Heifengshan and Shuangfengshan Fe (–Cu) deposits were probably IOCG deposits based on Re–Os ages of pyrite and C–O–S isotopes. Among these many genetic models, skarn and IOCG are currently the two major debated ore deposit types. These submarine volcanic-hosted deposits in northern Xinjiang commonly have skarn alteration and were therefore considered as skarn deposits (e.g., Bailingshan and Yamansu deposits; Mao et al., 2005), yet the absence of some typical skarn deposit features, including close relationships of orebodies with intrusions, carbonate host rocks, magmatic-derived ore-forming fluids, and (in some cases) garnet–pyroxene skarn alteration, has led these Fe (–Cu) deposits in northern Xinjiang to a local "submarine volcanic-hosted Fe (–Cu)" classification (Hou et al., 2014; Z.C. Zhang et al., 2014). Until recently, although some submarine volcanic-hosted deposits (e.g., Shaquanzi, Heifengshan and Shuangfengshan

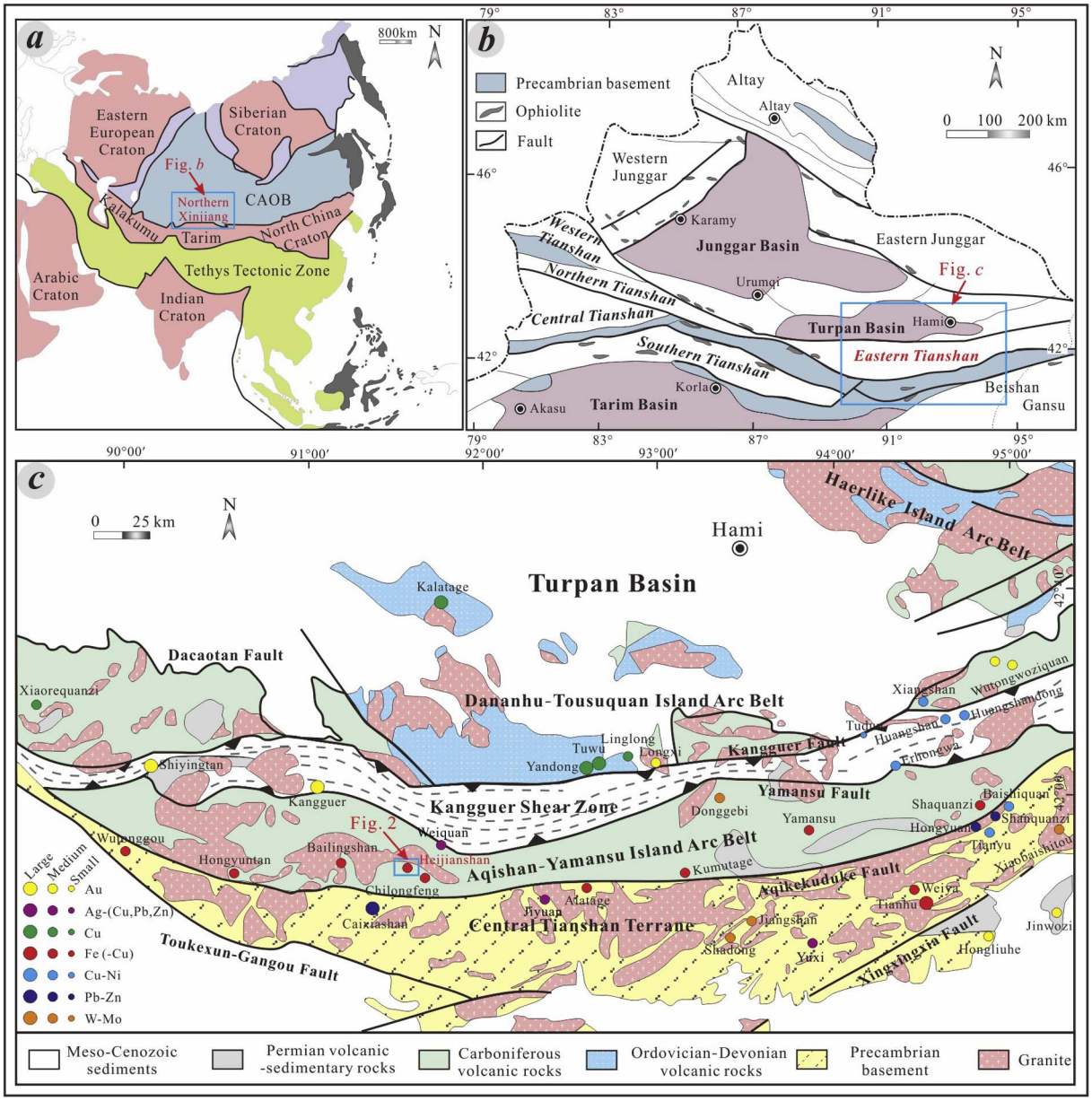

Fig. 1. (a). Simplified tectonic framework of the Central Asian Orogenic Belt (CAOB; simplified after Sengör and Natal'in, 1996); (b). Sketch map showing the tectonic framework of Northern Xinjiang (simplified after Chen et al., 2012); (c). Geologic map of the Eastern Tianshan Orogenic Belt and distribution of major ore deposits (simplified after Wang et al., 2006; Deng et al., 2014).

deposits; Huang et al., 2013c) have been proposed as IOCG type, yet detailed information of tectonic setting, ore deposit geology and systemic study of fluid evolution based on reliable paragenetic sequences are still lacking to support this hypothesis.

The Heijianshan Fe–Cu (–Au) deposit is a typical example of these Eastern Tianshan submarine volcanic-hosted Fe (–Cu) deposits. It was initially recognized as a medium-sized Cu deposit in Chinese classification (0.38 Mt ore @ 0.78 wt% Cu; XUARGS, 2003) but now with abundant magnetite, copper and/or even minor gold (in this study) after preliminary exploration, and initially mined as an iron deposit and abandoned now, has been rarely studied and poorly understood. In previous regional studies, the Heijianshan Fe–Cu (–Au) deposit was considered as a volcanic (Han et al., 2002; Pan et al., 2005; Liu, 2008; Wang et al., 2008), sedimentary deformation (Cui et al., 2008), volcanic sedimentary (Ma and Chen, 2011; Zhang, 2000) or skarn (Mao et al., 2005; Pirajno, 2013) deposit in Chinese Fe deposit classification without detailed anatomy of ore deposit, and the ore genesis and especially the characteristics of ore-forming fluids remain controversial. Furthermore, the differences of mineralization mechanisms between Fe and Cu were still unknown in this belt. Therefore, detailed study of the Heijianshan Fe–Cu (–Au) deposit may provide clues for understanding the ore deposit, and the genesis of Fe and Cu (–Au) mineralization in this important metallogenic belt in NW China.

In this paper, we present new data on the ore deposit geology, alteration and mineralization paragenesis, fluid inclusions and *in-situ* SIMS sulfur isotopes of the Heijianshan deposit to elucidate its ore-forming fluid source and evolution, and reveal its ore genesis, which can act as an important example for this important submarine volcanic-hosted Fe (–Cu) mineralization belt in NW China.

2. Regional geology

The CAOB, located between the Siberian, Tarim and North China cratons (Fig. 1a), is the largest Phanerozoic accretionary orogen in the world, and comprises Precambrian massifs, magmatic arcs, ophiolites and other accretionary complexes (Jahn et al., 2000, 2004; Windley et al., 2007). It was likely formed from the diachronous collisions between the Siberia and Tarim-Sino-Korean plates along the Solonker suture during the Carboniferous to Early Triassic (Gao et al., 1998; Charvet et al., 2007; Han et al., 2009; Xiao et al., 2009). The Eastern Tianshan Orogenic Belt (northern Xinjiang; Fig. 1a and b) is a key component of the CAOB and has a complex tectonic framework (Fig. 1b; Charvet et al., 2007; Xiao et al., 2008). The belt hosts many important ore deposits, e.g., Tuwu and Yandong Cu deposits, Shiyingtan and Kangguer Au deposits, Bailingshan, Heijianshan and Shaquanzi Fe (–Cu) deposits, and is thus one of the key areas for mineral exploration in NW China (Mao et al., 2005; Huang et al., 2013a).

The Eastern Tianshan contains three major tectonic units, i.e., (from north to south) the Dananhu-Tousuquan Island Arc Belt, Kangguer Shear Zone and Aqishan-Yamansu Island Arc Belt (or Back-arc Basin). These three units are separated by the regional E–W-trending Kangguer and Yamansu faults, respectively (Fig. 1c).

The Dananhu-Tousuquan Island Arc Belt consists predominantly of Ordovician–Permian volcanic and sedimentary rocks, as well as Devonian to Carboniferous intrusive rocks that host the large Tuwu-Yandong porphyry copper deposits (Mao et al., 2005). The Kangguer Shear Zone is mainly made up of greenschist-facies metamorphosed and ductile-deformed Carboniferous volcaniclastic rocks (Xiao et al., 2004), as well as Permian mafic–ultramafic intrusions (Mao et al., 2005). Moreover, abundant Au deposits (e.g., Shiyingtan and Kangguer) and Cu–Ni deposits (e.g., Huangshan and Huangshandong) were hosted in the western and eastern Kangguer Shear Zone, respectively (Fig. 1c).

The Aqishan-Yamansu belt is predominantly composed of Carboniferous and Permian volcanic/volcaniclastic and sedimentary rocks (Fig. 1c). The Carboniferous rocks comprise the Yamansu and Matoutan formations (Fig. 2). The Yamansu Formation is a ca. 5 km thick bimodal volcanic succession with three members in the northern part of the belt. The unconformably overlying Matoutan Formation, also called the Tugutubulake (Zhang et al., 2012) or Shaquanzi Formation (Mao et al., 2005) in the eastern part of the belt, contains two members in the southern part of the belt (Fig. 2). The Paleozoic volcanic-sedimentary sequences were intruded by numerous Carboniferous to Late Triassic granitoids, with ages from the Carboniferous to Late Triassic in back/intra-arc basin (350–325 Ma), basin inversion or arc-arc collisional (325–300 Ma), post-collisional (290–270 Ma) and within-plate (246–228 Ma) tectonic settings (Zhou et al., 2010; Zhang, 2012; Lei et al., 2013; Zhang et al., 2016). Major deposits discovered in this belt include Fe (e.g., Hongyuntan, Bailingshan, Chilongfeng, Yamansu), Fe–Cu (e.g., Heijianshan, Duotoushan, Shaquanzi) and Cu–Ag (e.g., Weiquan) deposits.

3. Deposit geology

The Heijianshan Fe–Cu (–Au) deposit is located at about 150 km south of Hami city, Xinjiang, NW China (Fig. 1c). Exposed rocks at Heijianshan are composed of the lower three members of the Upper Carboniferous Matoutan Formation, comprising (from bottom up) tuff and basalt, basalt, tuff and brecciated tuff, as well as basaltic andesite (Fig. 3). Orebodies commonly hosted by the tuff and brecciated tuff of the middle member, contain magnetite with epidote + amphibole + chlorite + carbonate + minor K-feldspar alterations, and/or chalcopyrite (–electrum) with chlorite alteration (Fig. 4).

The orebodies are tabular or stratiform (Fig. 4). The largest orebody, 30–50 m long and 8–10 m wide in the open pit, strikes 103° and dips 45° to the NE. Based on the different spatial distributions of Fe and Cu mineralization, ores can be divided into sulfide, oxide and mixed oxide-sulfide ores, with the latter two being predominant. Ore minerals include predominantly magnetite and hematite, with minor electrum and sulfides (pyrite, pyrrhotite and chalcopyrite). Gangue minerals include mainly epidote, calcite, amphibole and chlorite, with minor quartz, K-feldspar, sphene, apatite, albite, barite, tourmaline and sericite. Magnetite in the oxide and mixed oxide-sulfide ores commonly occurs as massive, disseminations, magnetite clasts, and minor veinlets. Meanwhile, pyrite and chalcopyrite (–electrum) in the sulfide and mixed oxide-sulfide ores occur mainly as disseminations and veinlets, and minor as massive. Most of the observed silicate and oxide minerals at Heijianshan are generally euhedral to subhedral, and metasomatic textures are common, indicating a possible hydrothermal origin.

The Matoutan Formation at Heijianshan was intruded by intermediate to felsic intrusive rocks (Fig. 3). Quartz syenite porphyry, quartz diorite and diorite porphyry with minor monzogranite mainly occur in the southern part of Heijianshan, whereas granodiorite with minor diorite porphyry are exposed in the northwestern part. Field relationships suggest that the quartz syenite porphyry, granodiorite and monzogranite were emplaced before diorite porphyry and quartz diorite, whilst diabase porphyry dykes were the youngest intrusive phase. Three fault systems and a small syncline were documented at Heijianshan: The oldest NW–NNW-trending faults cut the tuff, basalt and brecciated tuff sequences, the younger NNE–NE-trending faults crosscut quartz diorite locally, whereas the youngest E–NE-trending fault crosscuts diorite porphyry, quartz diorite, quartz syenite porphyry and monzogranite (Fig. 3).

4. Alteration/mineralization mineral paragenesis and chemistry

In this study, 110 doubly-polished thin sections from four drill holes (Fig. 4) were carefully observed for their alteration/mineralization paragenesis. Six alteration/mineralization stages have been established, including epidote alteration (Stage I), magnetite mineralization (Stage II), pyrite alteration (Stage III), Cu (-Au) mineralization (Stage IV), late veins (Stage V) and supergene alteration (Stage VI) (Fig. 5), largely based on textural relationships and mineral assemblages.

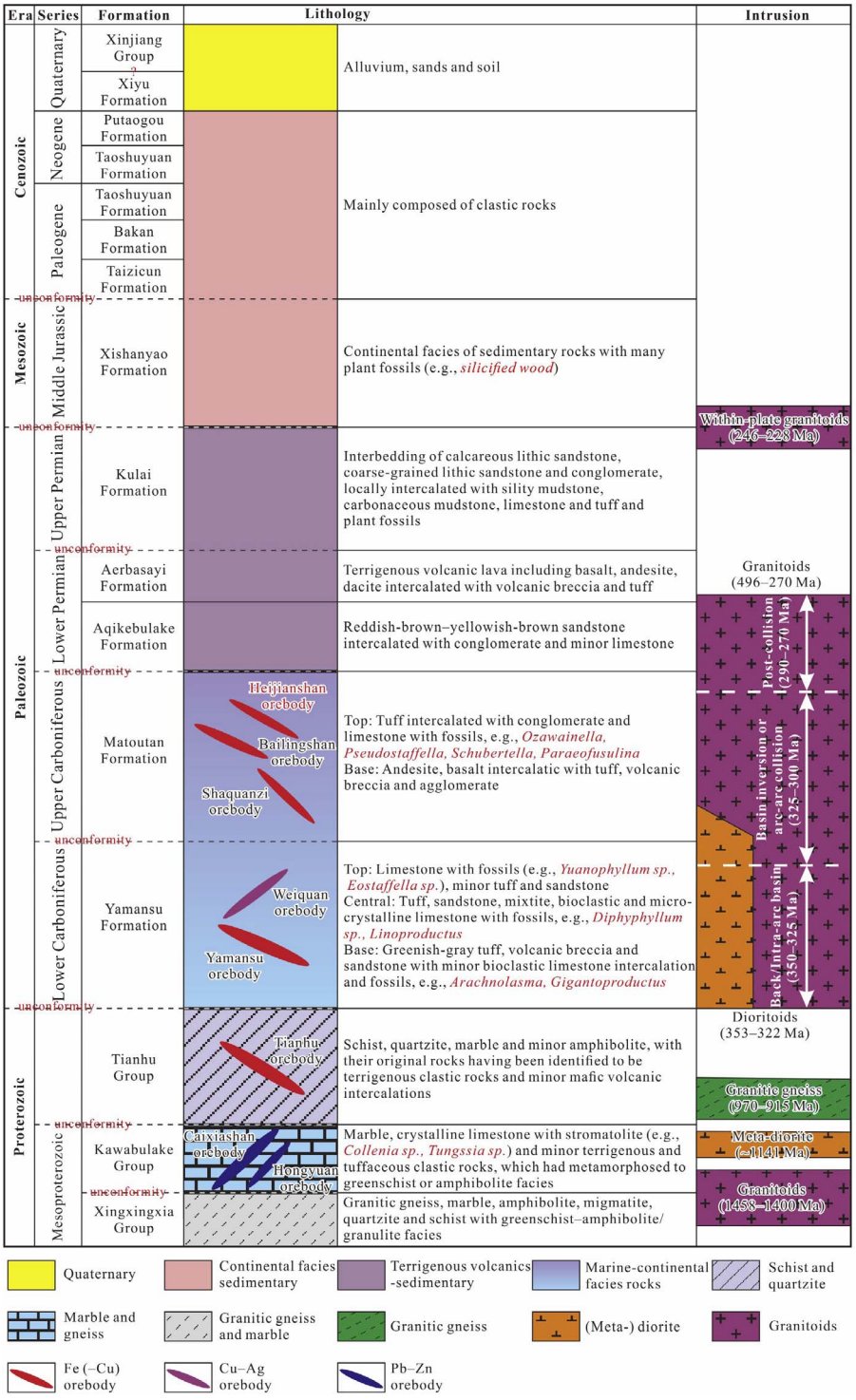

Fig. 2. Simplified stratigraphic column of the Eastern Tianshan region (including the Aqishan-Yamansu Island Arc Belt and Central Tianshan Terrane). References are from He et al. (2015), Huang et al. (2015a,b), Lei et al. (2011, 2013), Li et al. (2016), Liu et al. (2004), Wang et al. (2015), Xiu et al. (2002), Zhang (2012), Zhang et al. (2016), Zhou et al. (2010).

Representative electron probe microanalysis (EPMA) data of the alteration/mineralization minerals are given in Tables 1 and 2.

Stage I—Epidote alteration: Fine-grained yellow–green epidote is widespread in the host rocks, and commonly replaced plagioclase and amphibole phenocrysts in the tuff. The Heijianshan epidote is relatively Fe-rich, with the Fe/(Fe + Al) ratios ranging from 0.19 to 0.38 (Table 1). In this stage, epidote is widespread and can be coexisting with calcite in veins cutting altered Matoutan volcanic rocks (Fig. 6a). In some places, coarse euhedral epidote intergrows with calcite (which hosts the Stage I fluid inclusions) and is replaced by later-stage amphibole and fine-grained magnetite (Fig. 6b). Other Stage I minerals include tourmaline and sericite, and all those minerals may indicate a Ca–Mg alteration event before the Stage II magnetite and Stage IV Cu (–Au) mineralization.

Stage II—Magnetite/Fe mineralization: Magnetite, the main Heijianshan Fe mineral, is closely associated with amphibole (Fig. 6c–e). The fine-grained magnetite and amphibole accumulates commonly replaced or crosscut host rocks and the previous epidote, calcite and locally tourmaline (Fig. 6b–d). Magnetite in massive (Fig. 6e–g and k) and disseminated ores shows clear hydrothermal geochemical features: (a) depletions in Zr, Nb and Ta; (b) low Ti (< 2 wt%) and Al (< 1 wt%); and (c) Ni/Cr ≥ 1 (Zhao et al., 2016).

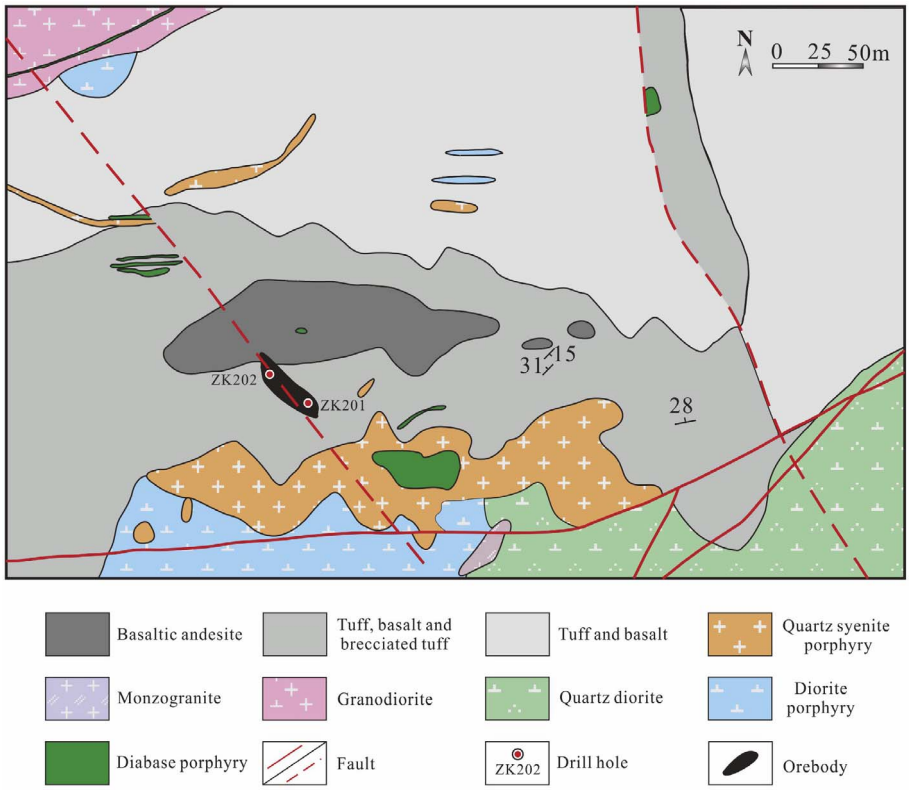

Fig. 3. Geologic map of the Heijianshan Fe–Cu (–Au) deposit (modified after XUARGS, 2003).

However, magnetite in the magnetite clasts ores has higher Cr concentrations than in other ore types, which may suggest earlier chromite geochemical inheritance (Zhao et al., 2016). Magnetite grains in those different ore types (i.e., massive, disseminations and magnetite clasts) can be distinguished by trace elements, e.g., diagrams of Cr vs. Co/Ni, Cr vs. Ti, V vs. Cr and Ni vs. Cr (Zhao et al., 2016). Stage II amphibole is classified as calcic amphibole in the Na_B vs. $(Ca + Na)_B$ diagram (Fig. 7a). The different amphibole sub-types in the Heijianshan deposit are distinguished by their Mg/(Mg + Fe) ratios, including tremolite (0.90–1.00), actinolite (0.73–0.90) and magnesiohornblende (0.77–0.95) (Table 1; Fig. 7b), which are also distinguishable by their morphology and color (e.g., crossed-polar). Locally, quartz, K-feldspar and sphene closely coexist with magnetite and amphibole. A hematite sub-stage (Stage II-A; Fig. 5), replaced subsequently by magnetite (i.e., "mushketovite"; Fig. 6f), may have occurred before the main magnetite mineralization (Stage II-B).

Stage III—Pyrite alteration: Major minerals include pyrite and quartz, and minor hematite, pyrrhotite and chalcopyrite, with different mineral assemblages of pyrite–hematite and pyrite–pyrrhotite–chalcopyrite to divide this stage into two sub-types (Fig. 5). Euhedral to subhedral Stage II magnetite grains were commonly replaced or cut by Stage III pyrite and Stage IV chalcopyrite (Fig. 6g–l). Pyrite commonly occurs as disseminations, massive or veinlets in sulfide and mixed oxide-sulfide ores (Fig. 6g–j). The Co/Ni ratios of pyrite vary from 0.24 to 39.91, and a few pyrite grains have their Ni contents below the EPMA detection limit. Meanwhile, pyrite, coexisting with pyrrhotite, was also crosscut by Stage IV chalcopyrite with electrum in veinlets (Fig. 6h and j). The subhedral pyrrhotite has higher Fe (57.48–57.64 wt%) and Ni (0.34–0.64 wt%) and lower S (38.95–39.50 wt%) than pyrite (Table 2), and has smoothly rounded grain boundaries with pyrite and chalcopyrite.

Stage IV—Cu (–Au) mineralization: Major minerals include quartz, chalcopyrite and chlorite, with minor hematite and electrum. Chalcopyrite, as disseminations or veins, replace or cut earlier-stage minerals (e.g., Stage II magnetite and Stage III pyrite; Fig. 6g–l). Meanwhile, chalcopyrite–electrum, chalcopyrite–chlorite and minor quartz–chalcopyrite–hematite veins cut massive pyrite and magnetite (Fig. 6j–l). Electrum was firstly identified at Heijianshan (and other Fe (–Cu) deposits in the Aqishan-Yamansu belt) in this study, and is euhedral and composed predominately of Au (82.21 wt%) and Ag (15.56 wt%), with less Fe, Co, Cu, S and Bi (Table 2). Using the chlorite geothermometer (Kranidiotis and Maclean, 1987), the Heijianshan chlorite (Fe/(Mg + Fe) = 0.28–0.40) has yielded Cu (–Au) mineralization temperatures of 172–291 °C (mean: ~240 °C; Table 1).

Stage V—Late veins: Late-stage hydrothermal veins (up to ~15 mm width) are abundant at Heijianshan, but their mutual age relationships are unclear. Epidote and calcite veins (Fig. 6m) are widespread, cutting host rocks and other mineral assemblages. Locally, veins of quartz (Fig. 6n), (specular) hematite, tourmaline, chlorite and albite crosscut host rocks and sulfides.

Stage VI—Supergene alteration: Supergene alteration is well-developed and preserved at Heijianshan. Hematite and limonite veins crosscut magnetite bodies, whilst chalcopyrite was commonly replaced by digenite, bornite, chalcocite and malachite along its grain margin. Other supergene Cu minerals, such as atacamite and chrysocolla (Fig. 6o), were also locally documented in the shallow open pit.

5. Fluid inclusions

Samples for fluid inclusion observation and microthermometry (Table 3) were chosen based on paragenetic relationships (Fig. 5) that reflect the nature and compositions of the ore-forming fluids. At Heijianshan, 22 doubly-polished thin sections were made from 17 quartz and calcite samples from the different alteration/mineralization stages to observe types, sizes, shapes, occurrences and vapor/liquid ratios of fluid inclusions under transmitted light. Among these samples, four thin sections were selected for scanning electron microscope-cathodoluminescene (SEM-CL) analysis, and 11 thin sections (from nine samples) were selected for microthermometric measurements. Although several minerals were examined, fluid inclusions were only

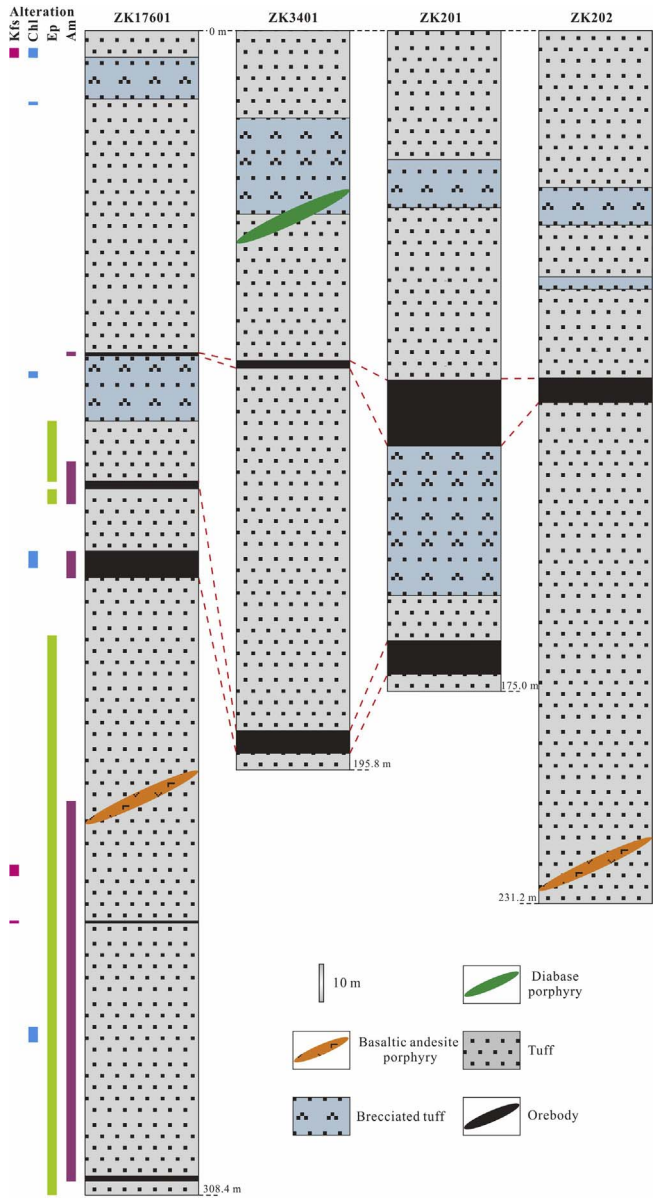

Fig. 4. Schematic stratigraphic columns of the Matoutan Formation in the Heijianshan Fe–Cu (–Au) deposit area. Abbreviations Abbreviations: *Am*: amphibole, *Chl*: chlorite, *Ep*: epidote, *Kfs*: K-feldspar.

found in calcite (Stage I and V) and quartz (Stage II-B and III-B) for the microthermometric study (Table 3). Fluid inclusions in Stage II-B and III-B quartz were used to represent the Fe mineralization and pyrite alteration stages, respectively. Due to the lack of suitable coexisting minerals and thus fluid inclusions, no direct microthermometric measurements were made for the Cu (–Au) mineralization stage.

5.1. Types of fluid inclusions

Microscopic petrography and CL imaging have found no clear evidence of inclusions being trapped along growth zones in either quartz or calcite crystals from Heijianshan Fe–Cu (–Au) deposit, and therefore the primary nature of these fluid inclusions cannot be confirmed only using the criteria of Roedder and Ribbe (1984) and Goldstein (2003). Many fluid inclusions at Heijianshan are distributed in three dimensions in the host crystals without clear crosscutting relationships (Fig. 8a) or in clusters probably as fluid inclusion assemblages (Fig. 8b; Goldstein and Reynolds, 1994; Goldstein, 2003) which can be used to distinguish groups of coevally-trapped inclusions.

Based on their phases at room temperature, only aqueous (W-type) and solid-bearing (S-type) fluid inclusions were identified at Heijianshan (Fig. 8). The W-type fluid inclusions commonly have a liquid phase with a bubble at room temperature (Fig. 8c). The S-type fluid inclusions have various sub-types, i.e., *Liquid-halite two-phase inclusions* (S_1-type; Fig. 8d), *Liquid-vapor-one transparent mineral three-phase inclusions* (S_2-type; Fig. 8e), *Liquid-vapor-two transparent minerals three-phase inclusions* (S_3-type; Fig. 8f–g), *Liquid-vapor-transparent-opaque minerals three-phase inclusions* (S_4-type; Fig. 8h), *Liquid-one opaque mineral two-phase inclusions* (S_5-type; Fig. 8i) and *Liquid-vapor-one opaque mineral three-phase inclusions* (S_6-type; Fig. 8j–k).

5.1.1. Aqueous fluid inclusions (W-type)

W-type inclusions are present in quartz and/or calcite veins of all the different ore-forming stages (Fig. 8a–c), accounting for 85% of the total population of the observed inclusions. They appear as two-phase at room temperature with an aqueous liquid and a vapor bubble (vapor/liquid ratios: 8–60 vol%), and show negatively crystalline, elliptical, regular or irregular shapes with sizes of 3–13 μm (quartz) and 3–25 μm (calcite) (Table 4). Primary fluid inclusions occur in isolation or as clusters. Some W-type inclusions occur linearly along the healing trail, but not across the crystal boundaries, suggesting that they are either primary or pseudosecondary.

5.1.2. Solid-bearing inclusions (S-type)

S-type inclusions have different sub-types which consist of a liquid and one/two daughter mineral(s) with/without vapor, but commonly with a liquid, a vapor phase and one daughter mineral at room temperature. Different inclusion sub-types may have different phases, such as *liquid-halite two-phase inclusions* (S_1-type; Fig. 8d) and *liquid–vapor-one transparent mineral three-phase inclusions* (S_2-type; Fig. 8e). Such inclusions (4–9 μm in size) commonly have regular/irregular shapes, found in Stage I to III quartz or calcite crystals, and account for about 10% of the total fluid inclusions (Tables 3 and 4). The daughter minerals include mainly cubic halite and in some cases rounded sylvite (L. Zhang et al., 2014) and anhydrite. The anhydrite-bearing mineral fluid inclusions (S_3-type) were observed in Stage II and III. Meanwhile, anhydrite-bearing inclusions (S_4-type) were only observed in Stage II. For S_5-type and S_6-type inclusions, opaque daughter minerals (probably chalcopyrite and pyrite) were observed in both Stage II and III (Fig. 8i–j). S_6-type inclusions contain red-colored daughter minerals, probably hematite and only observed in Fe mineralization stage (Fig. 8k). During the heating process, halite melting before or after the vapor bubble homogenized into the liquid or vapor by accident, but the opaque daughter minerals did not disappear.

5.2. SEM-CL analysis of quartz

SEM-CL analysis was conducted to differentiate the quartz from the main magnetite mineralization (Stage II) and pyrite alteration (Stage III) stages. SEM-CL imaging can reveal quartz textures that are invisible under optical microscopy or backscattered electron (BSE) imaging (Fig. 9a; Rusk and Reed, 2002), and these textures were used to determine the relative ages of the multiple quartz generations and coexisting vein minerals or fluid inclusion populations (Wilkinson et al., 1999; Rusk and Reed, 2002; Redmond et al., 2004; Allan and Yardley, 2007; Rusk et al., 2008). At Heijianshan, textures of Stage II and III quartz can be observed in the SEM-CL images and CL intensity is simplified as CL-dark, CL-gray and CL-bright in the following.

Stage II quartz veins show clear multiple generations, probably indicating multiple phases of fluid incursions (Fig. 9b and c). Stage II quartz has complex textures, including (a) CL-bright quartz cutting the less CL-bright quartz with various intensities (Fig. 9b); (b) cobweb texture (Fig. 9b); (c) CL-bright or CL-dark broken quartz with variable/blurry CL intensities (Fig. 9c); (d) euhedral growth zones of various

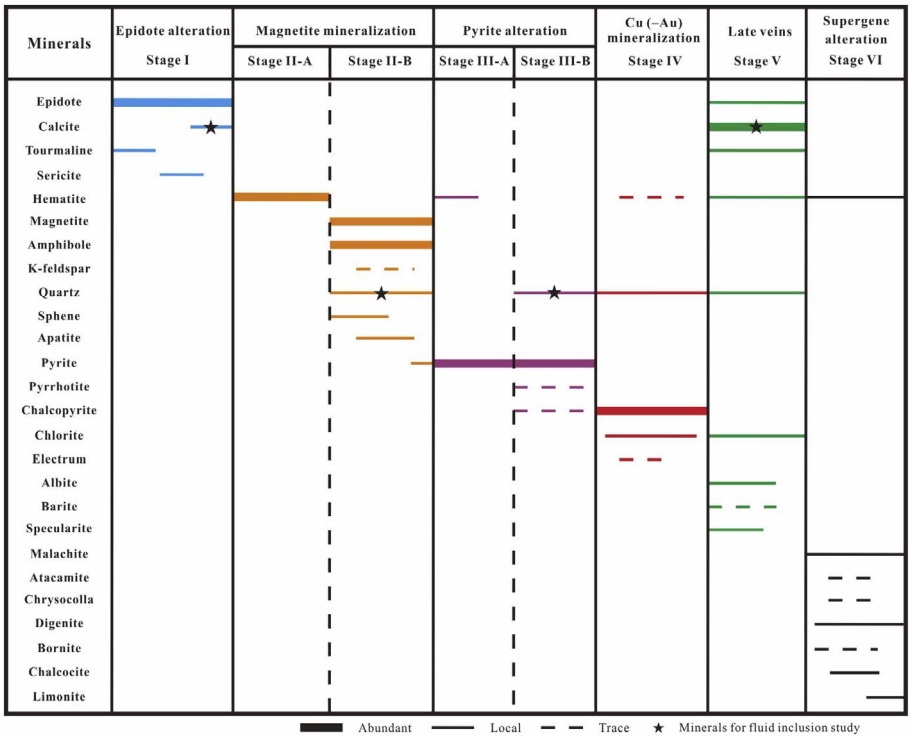

Fig. 5. Alteration and mineralization paragenesis of the Heijianshan Fe–Cu (–Au) deposit.

intensities to recrystallize the former generation of quartz (Fig. 9c); and (e) CL-dark fractures (Fig. 9b–d). These quartz textures indicate mechanical fracturing, recrystallization and growth in open space of quartz (Rusk and Reed, 2002), and from these two main generations of quartz can be distinguished, *viz.*, quartz2 (generation II) cut or recrystallized quartz1 (generation I) (Fig. 9b–c). In the pyrite alteration stage (Stage III), SEM-CL textures of quartz are similar to those in Stage II quartz. Dissolution of CL-bright quartz with CL-gray quartz and CL-dark fractures (Fig. 9d) are the main quartz textures of this stage.

5.3. Microthermometry

5.3.1. Stage I—epidote alteration

At Heijianshan, Stage I calcite (associated with epidote) hosts various fluid inclusion types, such as W-, S_1-, S_2- and S_3-type. The W-type fluid inclusions in calcite yield eutectic temperatures (T_e) of −73.2 °C to −22.1 °C, with mode at −60 °C (Fig. 10; Table 4). The final ice melting temperatures (T_m) are of −29.8 °C to −0.3 °C (Table 4), with the modes and corresponding salinities at −20 °C and 0 °C and 0.5–23.0 wt% NaCl equiv., respectively. These fluid inclusions were mostly homogenized to liquid (rarely to vapor) at 132–365 °C, with apparent peak at 240 °C (Fig. 10), while the calculated densities vary between 0.60 g/cm^3 and 1.14 g/cm^3 (Table 4).

Liquid-halite two-phase inclusions (S_1-type) and *Liquid-vapor-two transparent minerals three-phase inclusions* (S_3-type) were homogenized to liquid with the halite melting. One microthermometric S_1-type fluid inclusion has T_e = −61.6 °C, T_m = −22.3 °C and T_h (homogenization temperature) = 192 °C, while S_3-type fluid inclusion has T_h = 266 °C (no T_e and T_m measurement). The corresponding salinities (and densities) of S_1-type and S_3-type inclusions are 31.5 wt% NaCl equiv. (1.13 g/cm^3) and 35.7 wt% NaCl equiv. (1.10 g/cm^3), respectively. The T_e, T_m and T_h of S_2-type fluid inclusions are −70.2 °C to −57.6 °C, −32.8 °C to −0.2 °C and 179–370 °C, respectively, with the corresponding salinities and densities of 30.9–44.3 wt% NaCl equiv. and 1.08–1.13 g/cm^3 (Table 4). S_2-type fluid inclusions were mainly homogenized to liquid and rarely to vapor.

5.3.2. Stage II—Fe mineralization

Stage II quartz, which hosts many distinct fluid inclusion types, is mainly intergrown with massive magnetite and amphibole. The W-type fluid inclusions in Stage II quartz have T_e = −74.3 °C to −32.5 °C (modes at −60 °C and −35 °C) and T_m = −47.2 °C to −12.5 °C (modes at −35 °C and −20 °C) (Fig. 10). The corresponding salinities are 16.4–23.3 wt% NaCl equiv. (Table 4). These fluid inclusions have T_h of 101–536 °C with peak at 160 °C (Fig. 10), and are mostly homogenized to liquid and rarely to vapor. Their densities are within the range of 0.66–1.27 g/cm^3 (Table 4).

The Heijianshan Stage II quartz contains S_2-, S_4- and S_6-type inclusions, but the latter failed to yield homogenization temperatures. S_2-type inclusions yielded T_e = −70.8 °C to −35.8 °C, T_m = −28.3 °C to −21.5 °C and T_h = 170–471 °C, with the corresponding salinities and densities of 30.5–56.0 wt% NaCl equiv. and 1.08–1.14 g/cm^3, respectively (Table 4). These fluid inclusions were homogenized to liquid and rarely to vapor as W-type inclusions did. Meanwhile, S_4-type inclusions have T_e = −63.6 °C to −60.5 °C and T_m = −29.7 °C (Table 4). S_4-type and S_6-type fluid inclusions decrepitated before homogenization in the heating process at a maximum temperature of 421 °C, and the opaque minerals maintained a steady state during the heating process.

5.3.3. Stage III—pyrite alteration

W- and S_2-type inclusions were measured: For W-type inclusions, T_e = −81.3 °C to −51.3 °C (mode at −60 °C) and T_m = −52.4 °C to −15.4 °C (modes at −45 °C and −25 °C), and the corresponding salinities are 19.0–23.1 wt% NaCl equiv. (Fig. 10; Table 4). Meanwhile, these fluid inclusions were homogenized into liquid and seldom into vapor at 119–420 °C (mode at 170 °C; Fig. 10), and the corresponding densities were calculated to be 0.87–1.34 g/cm^3. S_2-type inclusions have T_e = −69.0 °C to −65.2 °C, T_m = −44.4 °C to −28.5 °C and T_h = 247–490 °C, with the corresponding salinities and densities of 34.5–58.4 wt% NaCl equiv. and 1.11–1.15 g/cm^3, respectively (Table 4).

5.3.4. Stage V—late veins

Only W-type fluid inclusions were observed in this stage (Fig. 8c),

Table 1
Representative EPMA data for the hydrothermal silicates from the Heijianshan deposit.

Mineral	Ep	Ep	Ep	Ep	Ep	Ep	Ep	Ep	Ep	Ep	Ep	Ep
Stage	Stage I	Stage I	Stage I	Stage I	Stage I	Stage I	Stage I	Stage I	Stage I	Stage I	Stage I	Stage I
Sample number	HJ13-027-2Ep-1	HJ13-027-2Ep-2	HJ13-027-4 Ep-1	HJ13-023(1)-1Ep-1	HJ13-023(1)-3Ep-1	HJ13-023(2)-3Ep-1	HJ13-023(2)-3Ep-2	HJ13-023(2)-2Ep-1	HJ13-023(3)-3Ep-2	HJ13-018-2Ep-1	HJ13-068-2Ep-1	HJ13-022-1Ep-1
SiO_2	37.55	38.41	37.65	40.52	37.94	38.30	38.75	38.41	38.09	37.56	37.89	37.97
TiO_2	0.00	0.00	0.01	0.00	0.00	0.04	0.05	0.01	0.51	0.03	0.07	0.02
Al_2O_3	19.35	21.32	20.35	21.91	21.76	25.49	24.06	24.30	21.83	21.40	21.21	23.12
Cr_2O_3	0.01	0.01	0.31	0.00	0.03	0.00	0.01	0.03	0.02	0.04	0.04	0.00
FeO^T	16.56	13.86	15.46	11.46	13.29	8.42	11.08	10.29	13.40	13.04	13.88	11.33
MnO	0.04	0.07	0.40	0.12	0.12	0.11	0.03	0.19	0.10	0.61	0.29	0.07
MgO	0.01	0.01	0.01	0.02	0.01	0.05	0.06	0.02	0.04	0.00	0.03	0.00
CaO	23.00	23.08	22.19	21.37	23.13	23.39	23.49	23.38	22.97	22.63	22.90	23.20
Na_2O	0.01	0.02	0.02	0.93	0.02	0.03	0.10	0.03	0.00	0.03	0.04	0.01
K_2O	0.01	0.00	0.01	0.01	0.04	0.01	0.02	0.01	0.02	0.02	0.01	0.00
P_2O_5	0.00	0.02	0.01	0.02	0.00	0.03	0.01	0.02	0.00	0.01	0.03	0.03
Total	96.55	96.79	96.41	96.35	96.33	95.87	97.65	96.69	96.97	95.36	96.37	95.75
Number of ions on the basis of 12.5 (O) and 8 cations												
Si	3.036	3.073	3.042	3.216	3.044	3.041	3.042	3.042	3.041	3.048	3.046	3.047
Ti	0.000	0.000	0.000	0.000	0.000	0.003	0.003	0.000	0.030	0.002	0.004	0.001
Al^{IV}	0.000	0.000	0.000	0.000	0.000	0.000	0.000	0.000	0.000	0.000	0.000	0.000
Al^{VI}	1.843	2.010	1.938	2.050	2.058	2.386	2.226	2.268	2.054	2.047	2.009	2.187
Cr	0.000	0.000	0.020	0.000	0.002	0.000	0.001	0.002	0.001	0.002	0.002	0.000
Fe^{3+}	1.087	0.843	0.960	0.659	0.860	0.527	0.700	0.647	0.804	0.855	0.890	0.711
Fe^{2+}	0.033	0.084	0.084	0.102	0.032	0.032	0.027	0.035	0.091	0.030	0.044	0.049
Mn	0.003	0.005	0.027	0.008	0.008	0.007	0.002	0.013	0.007	0.042	0.020	0.005
Mg	0.002	0.001	0.001	0.002	0.001	0.006	0.007	0.003	0.005	0.000	0.004	0.000
Ca	1.992	1.978	1.921	1.818	1.989	1.990	1.975	1.984	1.965	1.967	1.973	1.995
Na	0.002	0.003	0.004	0.143	0.003	0.005	0.015	0.005	0.000	0.004	0.006	0.001
K	0.001	0.000	0.001	0.001	0.004	0.001	0.002	0.001	0.002	0.002	0.001	0.000
P	0.000	0.001	0.001	0.001	0.000	0.002	0.001	0.001	0.000	0.001	0.002	0.002
Total	8.000	8.000	8.000	8.000	8.000	8.000	8.000	8.000	8.000	8.000	8.000	8.000
Fe/Fe + Al	0.38	0.32	0.35	0.27	0.30	0.19	0.25	0.23	0.30	0.30	0.32	0.26

Mineral	Tr	Act	Mg-Hb	Tr	Act	Mg-Hb	Tr	Mg-Hb	Tr	Tr
Stage	Stage II	Stage II	Stage II	Stage II	Stage II	Stage II	Stage II	Stage II	Stage II	Stage II
Sample number	HJ13-001-4Am-1	HJ13-001-4Am-2	HJ13-002-4Am-2	HJ13-002-4Am-3	HJ13-019(kuai)-3Am-1	HJ13-022-2Am-1	HJ13-022-5Am-1	HJ13-022-3Am-2	HJ13-023(1)-1Am-1	HJ13-027-1Am-1
SiO_2	53.68	53.39	51.51	54.01	53.01	52.29	53.82	51.73	52.32	52.94
TiO_2	0.00	0.08	0.05	0.09	0.02	0.62	0.43	0.50	0.18	0.32
Al_2O_3	3.33	3.42	4.83	2.64	3.67	4.33	3.10	4.94	3.87	3.73
FeO^T	9.77	10.69	12.61	9.43	11.42	8.73	8.54	8.72	9.96	8.51
MnO	0.15	0.16	0.17	0.13	0.25	0.15	0.18	0.13	0.25	0.18
MgO	17.13	16.82	15.22	18.41	15.98	17.59	17.84	17.71	16.87	18.04
CaO	12.30	12.62	12.76	12.67	12.57	12.40	12.46	12.79	12.69	12.70
Na_2O	0.27	0.30	0.46	0.28	0.33	0.46	0.32	0.52	0.39	0.48
K_2O	0.08	0.10	0.24	0.10	0.08	0.21	0.15	0.19	0.11	0.16
Total	96.70	97.58	97.83	97.75	97.33	96.79	96.83	97.23	96.64	97.06
Number of ions on the basis of 23 (O)										
Si	7.689	7.629	7.438	7.660	7.622	7.484	7.669	7.387	7.546	7.549
Al^{IV}	0.311	0.371	0.562	0.340	0.378	0.516	0.331	0.613	0.454	0.451
Al^{VI}	0.251	0.205	0.261	0.101	0.244	0.215	0.189	0.218	0.203	0.176
Ti	0.000	0.009	0.005	0.010	0.002	0.067	0.046	0.053	0.019	0.034
Fe^{3+}	0.925	0.875	0.768	0.843	0.881	0.835	0.918	0.766	0.829	0.815
Fe^{2+}	0.245	0.402	0.754	0.276	0.492	0.210	0.100	0.275	0.373	0.200
Mn	0.019	0.019	0.021	0.015	0.031	0.018	0.021	0.015	0.031	0.022
Mg	3.658	3.582	3.276	3.893	3.426	3.753	3.791	3.770	3.626	3.835
Ca	1.887	1.932	1.975	1.925	1.936	1.902	1.902	1.957	1.961	1.940
Na	0.076	0.082	0.127	0.076	0.092	0.127	0.088	0.144	0.109	0.133
K	0.014	0.019	0.045	0.018	0.015	0.038	0.027	0.035	0.021	0.030
Total	15.075	15.125	15.232	15.157	15.119	15.165	15.082	15.234	15.171	15.185
Mg/Mg + Fe	0.76	0.74	0.68	0.78	0.71	0.78	0.79	0.78	0.75	0.79

Table 1 *(continued)*

Mineral	Chl	Chl	Chl	Chl	Chl	Chl	Chl	Chl	Chl	Chl
Stage	Stage IV	Stage IV	Stage IV	Stage IV	Stage IV	Stage IV	Stage IV	Stage IV	Stage IV	Stage IV
Sample number	HJ13-005-4Chl-1	HJ13-005-4Chl-2	HJ13-019(kuai)-3Chl-1	HJ13-019(kuai)-3Chl-2	HJ13-068-3Chl-1	HJ13-068-4Chl-1	HJ13-069(1)-3Chl-1	HJ13-069(1)-3Chl-2	45	46
SiO_2	30.50	27.76	27.93	27.16	32.47	29.48	33.06	33.61	31.30	30.62
TiO_2	0.00	0.01	0.02	0.00	0.29	0.02	0.16	0.46	0.00	0.00
Al_2O_3	17.06	17.93	19.25	19.07	16.18	17.59	13.35	15.57	16.36	16.33
FeO^T	16.29	20.69	18.53	19.21	14.98	17.04	13.63	15.56	21.97	23.41
MnO	0.40	0.89	0.31	0.32	0.83	1.12	0.92	0.64	1.44	1.67
MgO	23.34	20.04	20.15	19.86	20.20	20.69	22.67	19.32	20.03	19.74
CaO	0.09	0.10	0.03	0.04	0.10	0.09	0.18	0.13	0.08	0.08
Na_2O	0.05	0.01	0.02	0.01	0.09	0.07	0.04	0.33	0.05	0.12
K_2O	0.08	0.01	0.02	0.01	2.79	0.13	0.09	2.87	0.05	0.04
Cr_2O_3	0.10	0.12	0.01	0.04	0.22	0.09	0.24	0.19	0.09	0.14
Total	87.91	87.54	86.26	85.72	88.14	86.33	84.34	88.68	91.37	92.14
Number of ions on the basis of 28 (O)										
Si	6.076	5.725	5.748	5.669	6.417	6.023	6.726	6.584	6.187	6.071
Al^{IV}	1.924	2.275	2.252	2.331	1.583	1.977	1.274	1.416	1.813	1.929
Al^{VI}	2.092	2.094	2.426	2.362	2.242	2.277	1.954	2.245	2.009	1.894
Ti	0.000	0.002	0.003	0.000	0.043	0.004	0.024	0.068	0.000	0.000
Cr	0.016	0.019	0.002	0.006	0.035	0.015	0.039	0.029	0.014	0.021
Fe^{3+}	0.086	0.000	0.095	0.017	0.113	0.153	0.417	0.190	0.109	0.000
Fe^{2+}	2.628	3.637	3.093	3.336	2.362	2.760	1.903	2.359	3.522	3.900
Mn	0.067	0.155	0.054	0.057	0.139	0.194	0.159	0.106	0.241	0.280
Mg	6.930	6.162	6.181	6.181	5.950	6.303	6.875	5.641	5.902	5.835
Ca	0.020	0.021	0.007	0.008	0.022	0.020	0.039	0.028	0.018	0.018
Na	0.037	0.006	0.015	0.010	0.065	0.056	0.031	0.251	0.038	0.092
K	0.040	0.004	0.012	0.006	1.409	0.068	0.044	1.433	0.024	0.018
Total	19.917	20.100	19.889	19.984	20.378	19.849	19.485	20.350	19.877	20.058
Fe/Fe + Mg	0.28	0.37	0.34	0.35	0.29	0.32	0.25	0.31	0.38	0.40
T (°C)	242.87	286.69	281.99	291.15	207.65	250.97	171.79	191.18	238.40	252.22

FeO^T as total iron. Temperature for chlorite calculated with $T/°C = 212Al^{IV} + 74.2[Fe/(Fe + Mg)] + 18$ (Kranidiotis and Maclean, 1987).

with their $T_e = -67.6$ °C to -17.8 °C (modes at -50 °C and -25 °C) and $T_m = -27.1$ °C to -0.2 °C (modes at -20 °C and -10 °C) and T_h = 46–343 °C (apparent peak at 160–180 °C), with the corresponding salinities of 0.4–23.2 wt% NaCl equiv. (Fig. 10). The W-type inclusions were mostly homogenized to liquid phase (rarely to vapor with occasional high vapor/liquid ratios). The corresponding densities were calculated to be 0.76–1.16 g/cm^3 (Table 4).

5.4. Filtering of overprinted fluid inclusions

Fluid overprinting is common in hydrothermal mineralization, especially in complex tectonic settings, e.g., the Eastern Junggar and Eastern Tianshan in NW China that experienced complex tectonic events during the Paleozoic (Gao et al., 1998; Charvet et al., 2007; Han et al., 2009; Xiao et al., 2009), which has been confirmed and reported

Table 2
Representative EPMA data for sulfides and electrum from the Heijianshan deposit.

Mineral	Py	Py	Py	Po	Ccp	Ccp	Elc	Bn	Cc
Stage	Stage II	Stage II	Stage III	Stage III	Stage IV	Stage IV	Stage IV	Stage VI	Stage VI
Sample number	HJ13-019(kuai)-4Py-1	HJ13-019(kuai)-4Py-2	HJ13-044(1)-3Py-1	HJ13-044(1)-5Po-1	HJ13-019(kuai)-4Ccp-2	HJ13-019-2Ccp-1	HJ13-019(kuai)-4Elc-1	HJ13-019-2Bn-1	HJ13-090(kuai)
Se	0.00	0.00	0.02	0.01	0.02	0.11	0.00	0.12	0.06
As	0.01	0.00	0.01	0.00	0.00	0.05	0.00	0.00	0.00
Fe	44.04	44.16	45.68	57.48	29.69	28.79	1.11	8.03	0.60
Co	2.06	1.87	0.07	0.07	0.11	0.02	0.02	0.01	0.00
Ni	0.00	0.00	0.24	0.34	0.00	0.00	0.00	0.00	0.00
Cu	0.00	0.00	0.01	0.05	33.73	34.63	0.29	68.52	79.23
Zn	0.02	0.00	0.01	0.01	0.00	0.00	0.00	0.00	0.00
Au	0.01	0.03	0.00	0.00	0.00	0.00	82.21	0.05	0.06
Ag	0.00	0.00	0.00	0.01	0.01	0.02	15.56	0.01	0.02
S	53.73	53.82	53.33	39.50	35.10	35.11	0.15	25.03	21.31
Pb	0.00	0.00	0.00	0.00	0.00	0.00	0.00	0.00	0.00
Bi	0.00	0.00	0.00	0.00	0.00	0.00	0.68	0.00	0.00
Total	99.89	99.89	99.36	97.47	98.68	98.74	100.00	101.76	101.27

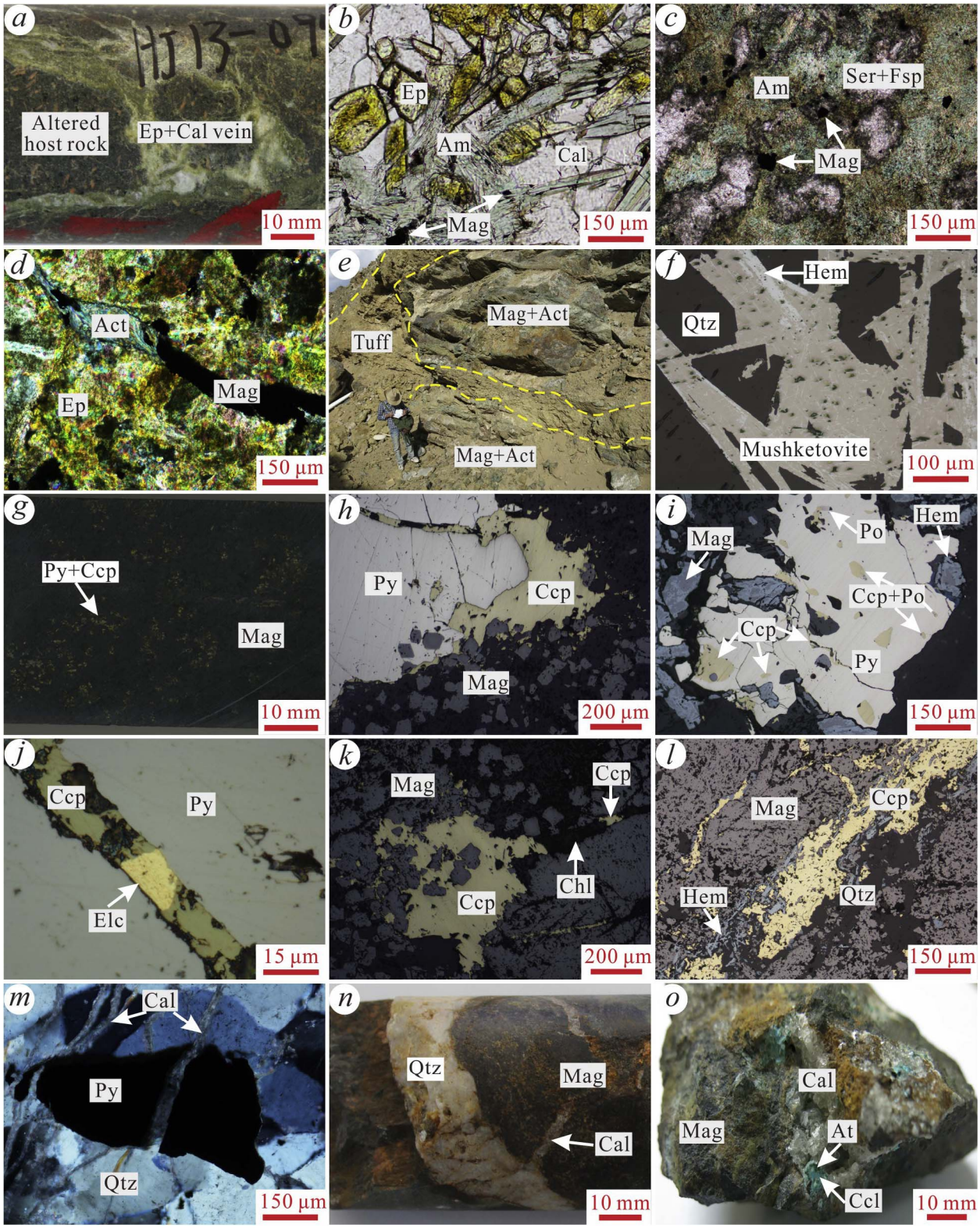

Fig. 6. Representative photographs of the Heijianshan alteration/mineralization paragenesis. (a). Epidote–calcite veins cutting altered host rock of the Matoutan Formation. (b). Epidote intergrown with calcite was replaced by euhedral amphibole and fine-grained magnetite. (c). Fine-grained amphibole and magnetite replaced sericite-altered host rocks. (d). Epidote cut by Stage II actinolite–magnetite vein. (e). Massive magnetite (with actinolite) orebody hosted by tuff of the Matoutan Formation. (f). Mushketovite intergrown with quartz, indicating a hematite sub-stage before the main Fe mineralization. Mushketovite replaced by supergene hematite. (g). Massive magnetite replaced by disseminated pyrite and chalcopyrite. (h). Euhedral magnetite wrapped by pyrite and chalcopyrite, and chalcopyrite veinlet cut pyrite. (i). Stage III disseminated pyrite intergrown with chalcopyrite and pyrrhotite to replace Stage II magnetite which was replaced by supergene hematite. (j) Stage III massive pyrite cut by a Stage IV chalcopyrite and electrum vein. (k). Magnetite replaced or cut by chalcopyrite ± chlorite veins. (l). Stage IV quartz–chalcopyrite–hematite vein cut massive magnetite. (m). Pyrite and quartz cut by late calcite veins. (n). Late quartz ± calcite vein cut magnetite mineralized host rocks. (o). Atacamite and chrysocolla of the supergene alteration stage. Abbreviations: *Act*: actinolite, *Am*: amphibole, *At*: atacamite, *Cal*: calcite, *Ccl*: chrysocolla, *Ccp*: chalcopyrite, *Chl*: chlorite, *Elc*: electrum, *Ep*: epidote, *Fsp*: Feldspar, *Hem*: hematite, *Mag*: magnetite, *Po*: pyrrhotite, *Py*: pyrite, *Qtz*: quartz, *Ser*: sericite.

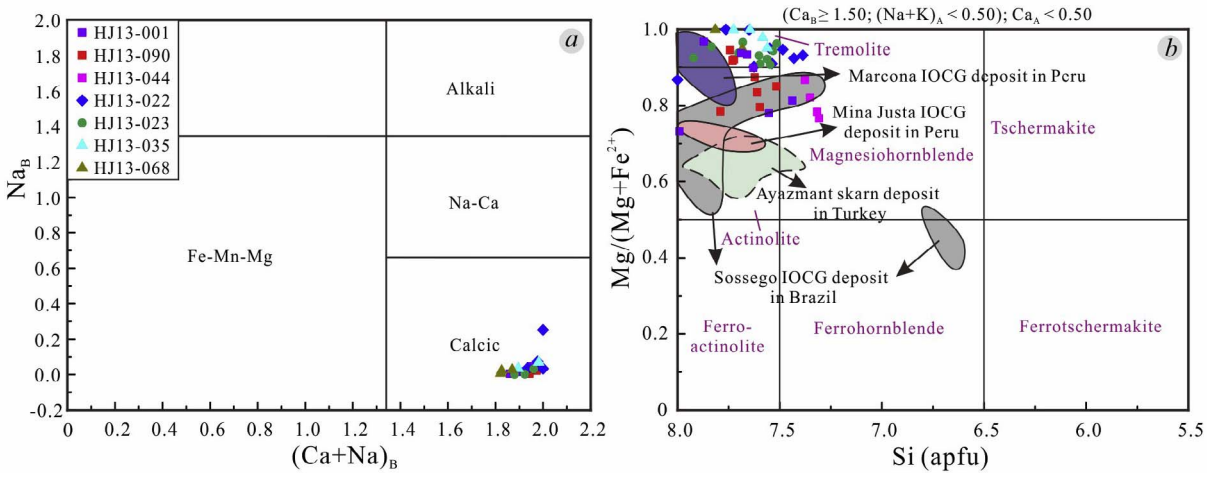

Fig. 7. (a). Na_B vs. $(Ca + Na)_B$ diagram, showing the Heijianshan amphibole data plotted in the calcic field. (b). Classification diagram for amphiboles (apfu) after Leake et al. (1997). Reference data: Marcona and Mina Justa IOCG deposits in Perú (Chen et al., 2010), Ayazmant Fe–Cu skarn deposit in Turkey (Oyman, 2010) and Sossego IOCG deposit in Brazil (Monteiro et al., 2008).

in recently published papers for hydrothermal deposits in NW China (Jiang et al., 2016; Wu et al., 2016) and Central Andes (e.g., Marcona and Mina Justa; Chen et al., 2011). In this study, we identified overprinted fluid inclusions at Heijianshan mainly based on their textures, T_h, T_e and T_m values.

Stage I fluid inclusions include both primary and secondary (probably overprinted from later stages) according to their microthermometric data from the primary-like fluid inclusion clusters (Table 4). The primary W-type inclusions have filling ratios of 8–50 vol% (mainly in 8–30 vol%), with T_h = 189–365 °C, T_e = −73.2 °C to −51.9 °C, T_m = −28.8 °C to −0.3 °C and corresponding salinities of 0.5–23.0 wt % NaCl equiv. The secondary W-type inclusions have filling ratios of 10–30 vol%, T_h = 132–229 °C T_e = −60.2 °C to −22.1 °C, T_m = −29.8 °C to −0.3 °C and corresponding salinities of 0.5–20.4 wt % NaCl equiv. (Table 4). The primary and secondary S_2-type inclusions have T_h, T_e, T_m and salinity of 223–370 °C and 179 °C, −70.2 °C to −57.6 °C and −68.5 °C, −32.8 °C to −7.0 °C and −0.2 °C, and 33.1–44.3 wt% NaCl equiv. and 30.9 wt% NaCl equiv., respectively (Table 4). Moreover, Stage I S_1- and S_3-type primary inclusions occur in isolation and have filling ratios of 15 vol% and 10 vol%, respectively. The measured S_1-type inclusion has T_h, T_e, T_m and salinity of 192 °C, −61.1 °C, −22.3 °C and 31.5 wt% NaCl equiv., respectively. S_3-type inclusion only yielded T_h = 266 °C and corresponding salinity of 35.7 wt% NaCl equiv. (Table 4). Therefore, Stage I hydrothermal fluids were featured by medium–high temperatures (189–370 °C), low T_e (−73.2 °C to −51.9 °C) and variable T_m (−32.8 °C to −0.3 °C), consistent with the reported H–O isotopes data and indicate interactions of the Late Carboniferous seawater and host rocks (Zhao et al., 2017b).

Fluid inclusions of Stage II and III have similar T_h, T_e and T_m, which probably indicates overprinted fluids of Stage III (and even Stage V) on Stage II (Fig. 10), consistent with our quartz CL results (Fig. 9). The few high temperature inclusions observed in Stage III may have been inherited from Stage II ones. Based on microthermometric and CL imaging results, fluid inclusions in these two stages can be divided into primary, secondary and inherited. In Stage II, primary fluid inclusions can be divided into the W-, S_2-, S_4- and S_6-type (Table 4). The Stage II W-type primary inclusions mainly occur in isolation or as clusters, and have filling ratios of 10–50 vol% (mainly 10–30 vol%), with T_h, T_e, T_m and corresponding salinities of 301–536 °C, −67.1 °C to −38.1 °C, −39.8 °C to −18.3 °C and 21.2–22.8 wt% NaCl equiv., respectively (Table 4). The S_2-type primary fluid inclusions are also mainly in isolation, with filling rations of 10 vol%. These fluid inclusions have T_h, T_e, T_m and salinity of 307–471 °C, −70.8 °C to −58.7 °C, −26.2 °C to −22.7 °C and 38.7–56.0 wt% NaCl equiv., respectively (Table 4). In addition, the primary S_4- and S_6-type fluid inclusions may be above 306 °C and 421 °C, respectively, because of the decrepitation occurred during the heating process. In summary, these primary fluid inclusions (both W- and S-type) indicate that Stage II fluids were of high temperatures (301–536 °C, also supported by oxygen isotope geothermometer of ~590 °C; Zhao et al., 2017b), medium–high salinities (21.2–22.8 wt% NaCl equiv. and 38.7–56.0 wt% NaCl equiv.), and low and variable T_e (−70.8 °C to −38.1 °C). However, Stage II secondary W- and S_2-type fluid inclusions occur mainly as clusters (minor in isolation) and have filling ratios of 7–60 vol% (mainly in 10–30 vol%) and 10–20 vol%, respectively. The secondary W- and S_2-type fluid inclusions have T_h, T_e, T_m and corresponding salinities of 101–292 °C and 170–281 °C, −74.3 °C to −32.5 °C and −54.9 °C to −35.8 °C, −47.2 °C to −12.5 °C and −28.3 °C to −21.5 °C, and 16.4–23.3 wt% NaCl equiv. and 30.5–36.8 wt% NaCl equiv., respectively (Table 4). In Stage III, fluid inclusions include primary and inherited ones, which correspond

Table 3
Location and types of fluid inclusions in the Heijianshan Fe–Cu (–Au) deposit.

Sample No.	Location	Paragenetic stage	Hosted mineral	Inclusion types
HJ13-075	Drill core ZK201; 150 m	Stage I	Calcite	W-type
HJ13-094	Drill core ZK202; 110 m	Stage I	Calcite	W-type (75%) + S_1-type (5%) + S_2-type (15%) + S_3-type(5%)
HJ13-001	Open pit	Stage II	Quartz	W-type (85%) + S_2-type (10%) + S_4-type (3%) + S_6-type(2%)
HJ13-003	Open pit	Stage II	Quartz	W-type (89%) + S_2-type (10%) + S_5-type(1%)
HJ13-093	Drill core ZK202; 100 m	Stage II	Quartz	W-type (95%) + S_2-type(5%)
HJ13-019	Drill core ZK17601; 140 m	Stage II	Quartz	W-type (95%) + S_2-type(5%)
HJ13-022	Drill core ZK17601; 150 m	Stage III	Quartz	W-type (80%) + S_2-type (10%) + S_3-type (5%) + S_5-type (2%) + S_6-type(3%)
HJ13-090	Drill core ZK202; 90 m	Stage III	Quartz	W-type (95%) + S_2-type (5%)
HJ13-090	Drill core ZK202; 90 m	Stage V	Calcite	W-type
HJ13-096	Drill core ZK202; 160 m	Stage V	Calcite	W-type

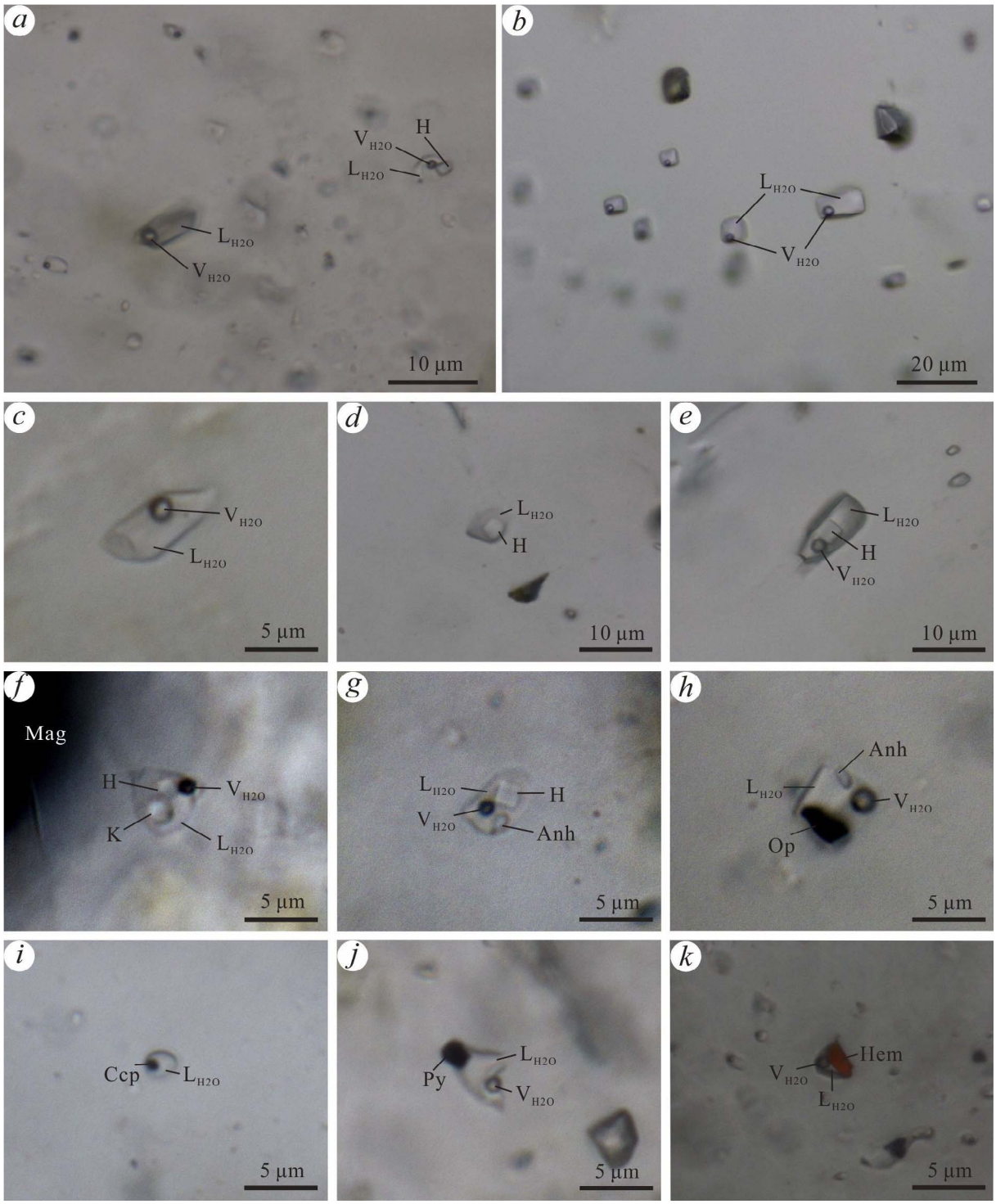

Fig. 8. Fluid inclusion types in the Heijianshan Fe–Cu (–Au) deposit. (a). W- and S-type fluid inclusions distributed in three dimensions in quartz crystal. (b). W-type fluid inclusion assemblages hosted by calcite. (c). W-type fluid inclusions in Stage I and II to Stage III and V. (d) S_1-type fluid inclusions in Stage I and II. (e). S_2-type fluid inclusions bearing halite in Stage I to III. (f). S_3-type fluid inclusions in Stage I–III, with halite and sylvite. (g) S_3-type fluid inclusions with halite and anhydrite in Stage II and III. (h). S_4-type fluid inclusions in Stage II with unclassified opaque daughter mineral. (i). S_5-type fluid inclusions with chalcopyrite in Stage II and III. (j). S_6-type fluid inclusions in Stage II and III with pyrite (opaque). (k). S_6-type fluid inclusion with hematite only observed in Stage II. Abbreviations: *Anh*: anhydrite, *Ccp*: chalcopyrite, *H*: halite, *Hem*: hematite, *K*: sylvite, *Mag*: magnetite, *Op*: opaque, *Py*: pyrite.

to low (119–262 °C) and high temperatures (315–490 °C), respectively. The Stage III primary fluid inclusions also can be divided into W- and S_2-type, having corresponding T_h, T_e, T_m and salinity of 119–262 °C and 247–250 °C, −81.3 °C to −51.3 °C and −69.0 °C to −67.7 °C, −52.4 °C to −15.4 °C and −32.7 °C to −28.5 °C, and 19.0–23.1 wt% NaCl equiv. and 34.5–34.7 wt% NaCl equiv., respectively (Table 4), which are similar to those of Stage II secondary fluid inclusions with $T_e < -45$ °C (those Stage II secondary fluid inclusions with $T_e > -45$ °C may indicate fluids of Stage V, but need further evidence to support; Fig. 10). The Stage III inherited fluid inclusions also contain W- and S_2-type, with their corresponding T_h, T_e, T_m and salinity of 315–420 °C and 490 °C, −67.9 °C to −59.4 °C and −65.2 °C, −38.0 °C to −29.6 °C and −44.4 °C, and 28.4 wt% NaCl equiv. and 58.4 wt% NaCl equiv., respectively (Table 4), which are similar to those Stage II primary fluid

Table 4
Summary of fluid inclusion petrography and microthermometric data for the Heijianshan Fe–Cu (–Au) deposit.

Stage	Mineral	Types	Size (μm)	Filling (vol. %)	$T_{homogenization}$ (°C)			$T_{final\ ice\ melting}$ (°C)			$T_{eutectic}$ (°C)			Salinity (wt.%)			Density (g/cm^3)		
					Min	Max	n	Min	Max	n	Min	Max	n	Min	Max	n	Min	Max	n
Stage I	Cal	W (Primary)	4–18	8–50	189	365	60	−28.8	−0.3	52	−73.2	−51.9	50	0.5	23.0	34	0.60	1.07	52
		W (Secondary)	3–8	10–30	132	229	12	−29.8	−0.3	11	−60.2	−22.1	8	0.5	20.4	6	0.87	1.14	11
		S_1 (Primary)	6	15	192		1	−22.3		1	−61.6		1	31.5		1	1.13		1
		S_2 (Primary)	5–9	8–25	223	370	14	−32.8	−7.0	11	−70.2	−57.6	10	33.1	44.3	14	1.08	1.12	14
		S_2 (Secondary)	6	25	179		1	−0.2		1	−68.5		1	30.9		1	1.13		1
		S_3 (Primary)	9	10	266		1							35.7		1	1.10		1
Stage II	Qtz	W (Primary)	3–6	10–50	301	536	23	−39.8	−18.3	18	−67.1	−38.1	14	21.2	22.8	4	0.66	1.04	14
		W (Secondary)	3–13	7–60	101	292	131	−47.2	−12.5	125	−74.3	−32.5	97	16.4	23.3	27	0.92	1.27	125
		S_2 (Primary)	5–8	10	307	471	4	−26.2	−22.7	4	−70.8	−58.7	3	38.7	56.0	4	1.08	1.13	4
		S_2 (Secondary)	4–6	10–20	170	281	4	−28.3	−21.5	3	−54.9	−35.8	3	30.5	36.8	4	1.10	1.14	4
		S_4 (Primary)	4–8	10–15	> 306		2	−29.7		1	−63.6	−60.5	2						
		S_6 (Primary)	4	10	> 421		1												
Stage III	Qtz	W (Primary)	3–13	8–30	119	262	89	−52.4	−15.4	80	−81.3	−51.3	60	19.0	23.1	11	1.02	1.34	80
		W (Inherited)	4–5	30	315	420	2	−38.0	−29.6	2	−67.9	−59.4	2	28.4		1	0.87	1.04	2
		S_2 (Primary)	4–5	10–20	247	250	2	−32.7	−28.5	2	−69.0	−67.7	2	34.5	34.7	2	1.11		2
		S_2 (Inherited)	5	10	490		1	−44.4		1	−65.2		1	58.4		1	1.15		1
Stage V	Cal	W (Primary)	4–25	5–20	46	198	128	−27.1	−0.2	113	−67.3	−17.8	87	0.4	23.2	92	0.94	1.16	112
		W (Inherited)	4–15	10–30	201	343	36	−24.8	−0.3	23	−67.6	−19.1	18	0.5	23.2	20	0.76	1.04	23

Stage II S_4-type and S_6-type inclusions were not shown in the figures. Salinities were calculated using the NaCl–H_2O system (Bodnar, 1993). W-type inclusions with salinities over 23.3 wt % NaCl equivalent were not included in this paper, because they should equal to halite saturation in the NaCl–H_2O system and may represent metastable at room temperature. But during heating or cooling processes, such W-type inclusions with salinities over 23.3 wt% NaCl equiv. didn't have any daughter-bearing minerals, therefore, these salinities can not represent the true salinity of fluids.
Abbreviations: *Cal*: calcite; *Qtz*: quartz.

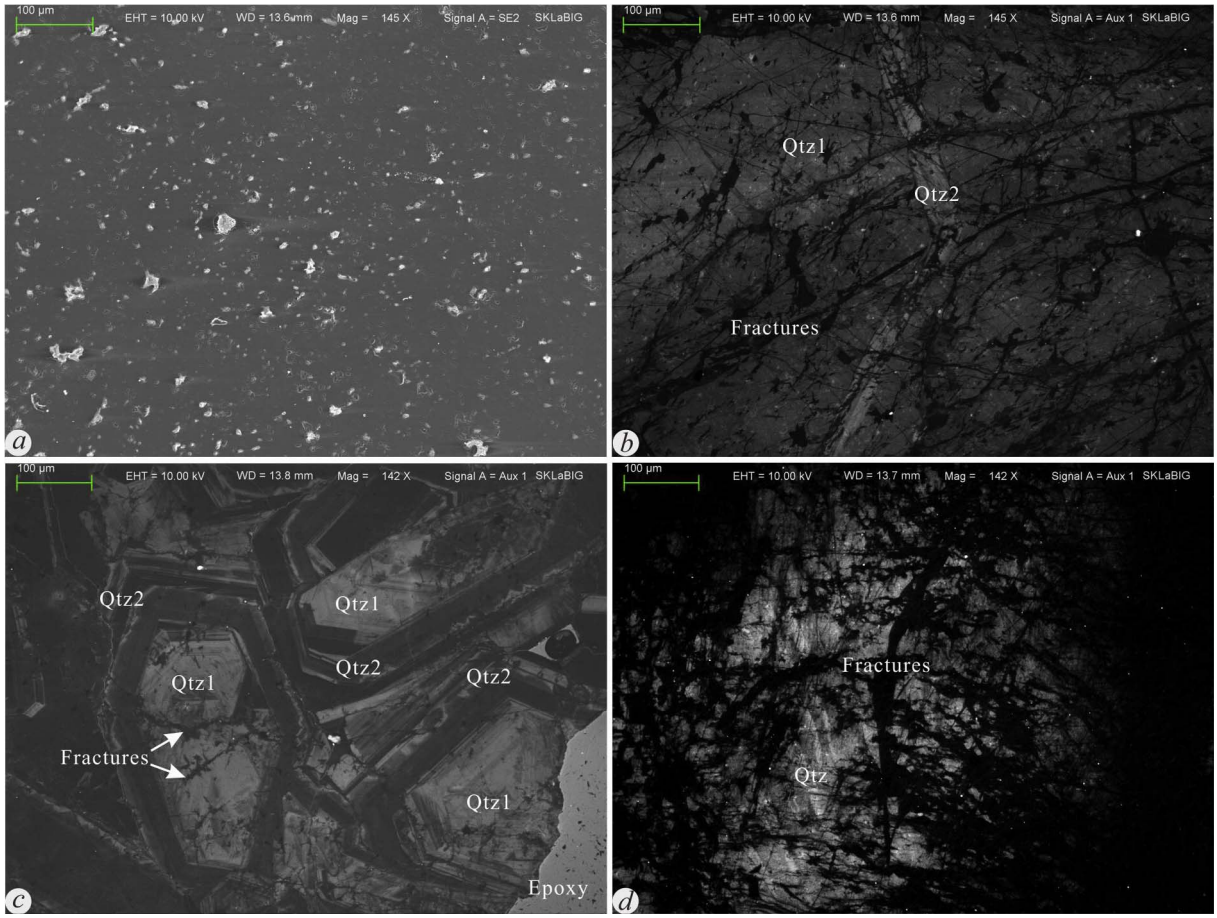

Fig. 9. SEM-CL of quartz in Stage II (a–c) and III (d). (a). BSE of b for quartz in magnetite mineralization stage. (b). CL-bright quartz with various intensities cut by CL-dark fractures and CL-bright quartz. (c). CL-bright or CL-dark broken quartz with blurred CL intensity recrystallized by euhedral quartz. (d). Dissolution of CL-bright and CL-gray quartz cut by CL-dark fractures in Stage III.

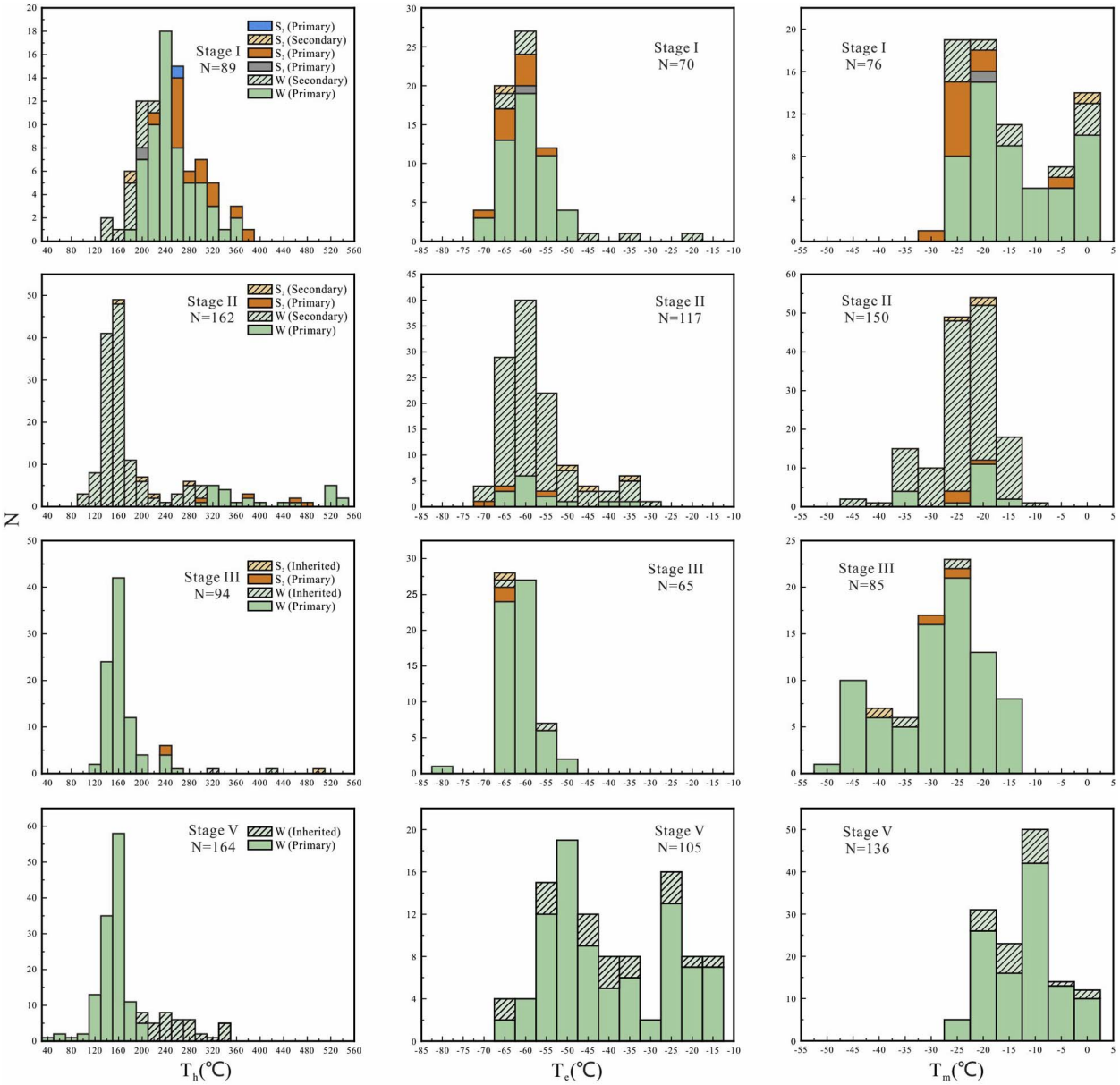

Fig. 10. Histograms of homogenization temperature (T_h), eutectic temperature (T_e) and final ice melting temperature (T_m) for the fluid inclusions in the different-stage Heijianshan minerals.

inclusions. Hence, the Stage III fluids were featured by low temperatures (119–262 °C), medium–high salinities (19.0–23.1 wt% NaCl equiv. and 34.5–34.7 wt% NaCl equiv.) and low T_e (−81.3 °C to −51.3 °C; Fig. 10; Table 4).

Although Stage V fluid inclusions have similar T_h peaks to those of the main magnetite mineralization (II-B) and pyrite alteration (III) stages, distinct T_e and T_m peaks are present (Fig. 10) to distinguish Stage V fluids from fluids of the other stages. In Stage V, the fluid inclusion-hosting calcite replaced/cut the Stage II ore-hosting rocks and Stage III quartz–pyrite assemblage, and may have inherited the earlier-stage high-temperature fluid inclusions. Moreover, some fluid inclusions in Stage V calcite occur in isolation (minor as clusters) and have relatively high T_h (> 200 °C), which are quite different from the predominantly low temperature (peak at ~160 °C) fluid inclusions that represent the late-hydrothermal activities at Heijianshan. Therefore, Stage V fluid inclusions can be divided into inherited ones with relatively high temperatures (> 200 °C) and primary ones with low temperatures (peak at ~160 °C). The primary W-type fluid inclusions occur as clusters and have filling ratios of 5–20 vol%, with T_h, T_e, T_m and corresponding salinities of 46–198 °C, −67.3 °C to −17.8 °C, −27.1 °C to −0.2 °C and 0.4–23.2 wt% NaCl equiv., respectively, whilst the inherited W-type fluid inclusions have filling ratios of 10–30 vol%, with their corresponding T_h, T_e, T_m and corresponding salinities of 201–343 °C, −67.6 °C to −19.1 °C, −24.8 °C to −0.3 °C and 0.5–23.2 wt% NaCl equiv., respectively (Table 4). Therefore, Stage V fluids were featured by low temperature (~160 °C) with variable T_e (−67.6 °C to −17.8 °C) and T_m (−27.1 °C to −0.2 °C) (Fig. 10; Table 4).

6. Sulfur isotopic geochemistry

The sulfur isotopic compositions ($\delta^{34}S$ values) of one Stage II pyrite (three spots), five Stage III pyrite (23 spots) and one Stage III chalcopyrite (three spots), and two Stage IV chalcopyrite (14 spots) were *in-situ* SIMS analyzed. The mineral assemblages, textures and sulfur isotopic results of these sulfides are illustrated in Figs. 11 and 12 and listed in Table 5.

The measured Stage II subhedral disseminated pyrite (coexist with

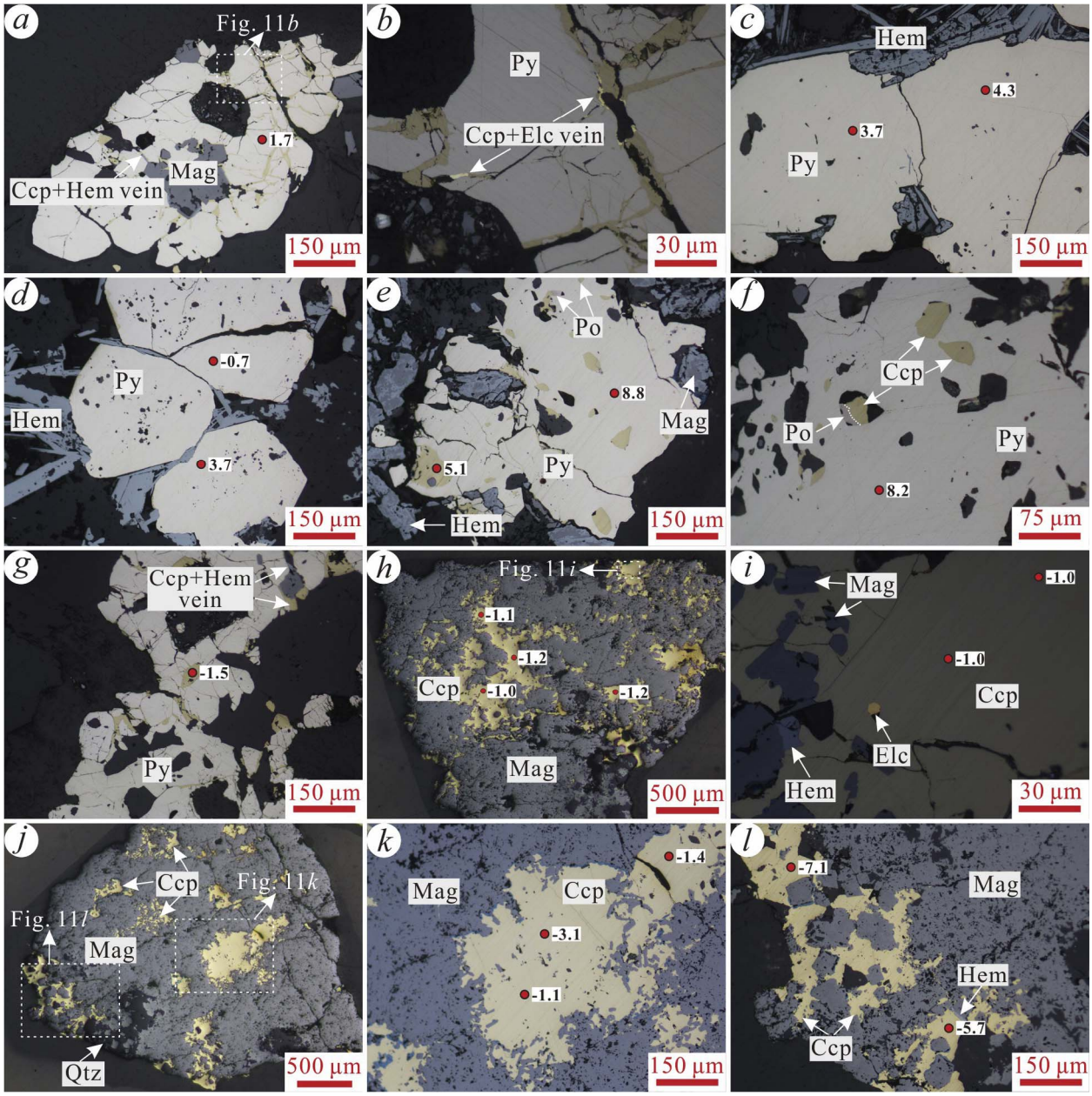

Fig. 11. Typical sulfide mineral assemblages, textures and SIMS analysis results from Stage II to IV in the Heijianshan Fe–Cu (–Au) deposit. (a). Stage II disseminated pyrite and euhedral to subhedral magnetite cut by Stage IV chalcopyrite ± hematite ± electrum veins. (b). Stage II pyrite cut by Stage IV chalcopyrite–electrum veins. (c and d). In Stage III, subhedral Type A pyrite with hematite shows variable $\delta^{34}S$ values, and some Type A pyrite grains were inclusion-rich. (e and f). In Stage III, disseminated Type B pyrite–chalcopyrite ± pyrrhotite replaced Stage II magnetite which was replaced by Stage VI hematite. (g). Disseminated Stage II pyrite replaced/cut by Stage IV chalcopyrite ± hematite veins. (h). Disseminated Stage IV chalcopyrite (with narrow $\delta^{34}S$ range) replaced Stage II massive magnetite. (i). Stage II magnetite replaced by homogeneous Stage IV chalcopyrite intergrown with electrum + hematite. (j–k). Massive Stage II magnetite replaced by Stage IV chalcopyrite. (l). Disseminated Stage IV chalcopyrite ± hematite (with relatively low $\delta^{34}S$ values) replaced Stage II magnetite. Red circles with numbers show SIMS point analysis and $\delta^{34}S$ values, respectively. Abbreviations: *Cal*: calcite, *Ccp*: chalcopyrite, *Elc*: electrum, *Hem*: hematite, *Mag*: magnetite, *Po*: pyrrhotite, *Py*: pyrite. (For interpretation of the references to colour in this figure legend, the reader is referred to the web version of this article.)

Stage II magnetite and cut by Stage IV chalcopyrite + hematite veins; Fig. 11a and b) has $\delta^{34}S$ values of 1.7–4.3‰, averaging 2.6‰ (Table 5). The measured Stage III pyrite grains can be grouped into two types, i.e., those coexist with euhedral hematite (Type A; Fig. 11c and d) or with chalcopyrite–pyrrhotite (Type B; Fig. 11e and f). Type B pyrite has higher $\delta^{34}S$ values (4.6–10.0‰; average 6.6‰) than those of Type A (−0.7–4.3‰; average 2.5‰), and its coexisting chalcopyrite has $\delta^{34}S$ values of 5.1–6.1‰ (average to 5.6‰; Table 5). The analyzed Stage IV chalcopyrite ($\delta^{34}S$ = −7.1‰ to −0.9‰) occurs as disseminations or (± electrum ± hematite) veins to replace or cut earlier-stage pyrite/magnetite (Fig. 11g–l; Table 5). Two analytical spots with relatively low $\delta^{34}S$ values (−7.1‰ and −5.7‰; Fig. 11l) are located in the sulfide rim with rough surface, which likely made the analytical results less reliable (Kita et al., 2009; Evans et al., 2014). Hence, Stage IV chalcopyrite contains $\delta^{34}S$ values of −3.5‰ to −0.9‰, averaging −1.5‰ (Table 5).

$\delta^{34}S$ values of the hydrothermal fluids could be estimated from the $\delta^{34}S$ values of sulfides and sulfates with the oxygen fugacity (fO_2) and temperature conditions during mineral precipitation (Ohmoto and Rye, 1979; Ohmoto and Goldhaber, 1997). In Stage II, the analyzed pyrite was intergrown with magnetite (Fig. 11a), indicating relatively high fO_2 and temperature (~590 °C by the magnetite–actinolite oxygen isotope geothermometer; Zhao et al., 2017b) and negligible $\delta^{34}S$ difference in the sulfides and fluids (Table 6). Therefore, the $\delta^{34}S$ values of Stage II

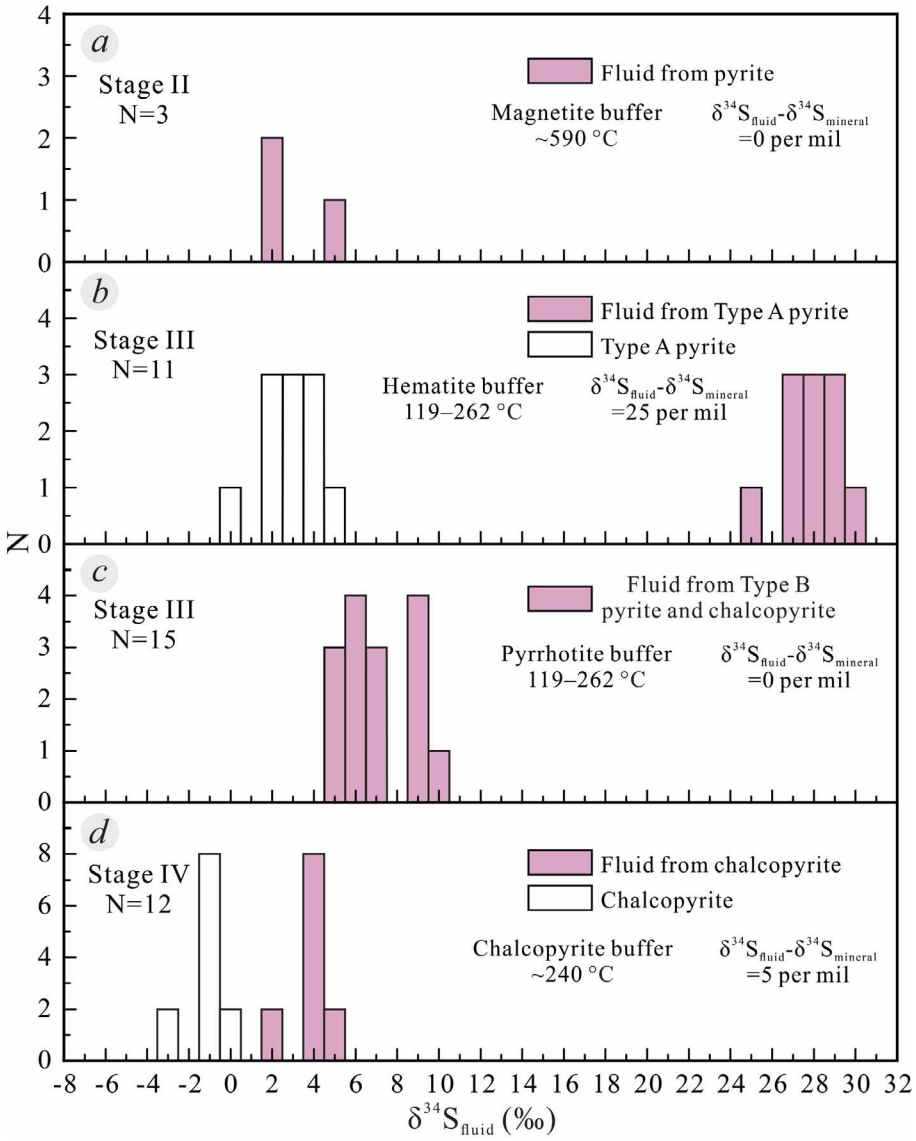

Fig. 12. $\delta^{34}S_{fluid}$ values of Stage II to IV sulfides and calculated ore-forming fluids in the Heijianshan Fe–Cu (–Au) deposit.

pyrite can represent those of the Stage II hydrothermal fluids, i.e., 1.7–4.3‰ (Fig. 12a; Table 6).

In Stage III, the analyzed Type A and Type B pyrite were intergrown with hematite and pyrrhotite–chalcopyrite, respectively (Fig. 11c–f), indicating rapid fO_2 drop. Temperatures determined from microthermometry are 119–262 °C (peak at 170 °C; Table 6). In low–medium temperatures, the $\delta^{34}S$ conversion factor ($\Delta = \delta^{34}S_{H2S} - \delta^{34}S_{fluid}$) are about −25‰ (for Type A pyrite) and 0‰ (for Type B pyrite–chalcopyrite) (Ohmoto and Goldhaber, 1997), and therefore the Type A and Type B (with its coexisting chalcopyrite) $\delta^{34}S_{fluid}$ values are 24.3–29.3‰ (peak at ~27–29‰) and 4.6–10.0‰ (peak at ~6‰ and 9‰; Fig. 12b and c; Table 6), respectively.

In the Cu (–Au) mineralization stage (Stage IV), although chalcopyrite was intergrown with quartz, chlorite, with minor electrum and hematite (Fig. 6j–l), the measured disseminated chalcopyrite was associated with a lesser amount of hematite than in Stage III Type A pyrite (Fig. 11g–l). Hence, the chalcopyrite buffer is valid, and the $\delta^{34}S$ conversion factor ($\Delta = \delta^{34}S_{H2S} - \delta^{34}S_{fluid}$) at medium–low temperatures (172–291 °C (average 242 °C) as constrained by the chlorite geothermometer; Table 1) is about −5‰ (Ohmoto and Goldhaber, 1997). The Stage IV $\delta^{34}S_{fluid}$ values are 1.5–4.1‰ (peak at ~4‰; Fig. 12d; Table 6).

7. Discussion

7.1. Sources of sulfur and metals

At Heijianshan, Stage II pyrite shows relatively low $\delta^{34}S$ values (1.7–4.3‰; Figs. 12a and 13a), which are inconsistent with a mantle source ($\delta^{34}S = 0 \pm 1$‰; Eldridge et al., 1991) but well consistent with magmatic source ($\delta^{34}S = 0 \pm 5$‰; Ohmoto and Goldhaber, 1997). The possibility of a magmatic–hydrothermal origin for the Heijianshan Fe mineralization is also supported by the published oxygen isotope data (Zhao et al., 2017b). In Stage III, the Type A pyrite $\delta^{34}S_{fluid}$ values (24.3–29.3‰) are much higher than those of typical magmatic–hydrothermal reservoirs and Late Carboniferous seawater (about 13–19‰; Fig. 13), but comparable with an evaporite source (about 10–26‰; Hoefs, 1997; Fig. 13a). Considering the probable Carboniferous back-/intra-arc basin (~350–325 Ma) and basin inversion (~325–300 Ma) settings of the Aqishan-Yamansu belt (Zhang et al., 2016), basinal brines (derived from residual seawater during basin closure) may have been responsible for the Type A pyrite–hematite alteration, consistent with the low temperature (< 300 °C), Ca–Mg-dominated and medium–high salinity characteristics of the Stage III fluids. Stage III Type B pyrite and chalcopyrite (with pyrrhotite) were likely generated from the fluids with high $\delta^{34}S_{fluid}$ values (4.6–10.0‰).

Table 5
Sulfur isotopic compositions of minerals from the Heijianshan Fe–Cu (–Au) deposit.

Sample	Stage	Mineral	$\delta^{34}S_{V\text{-}CDT}$ (‰)	Comment
HJ-019kuaiPY@01	Stage II	Pyrite	4.3	Disseminated Stage II pyrite intergrows with euhedral to subhedral magnetite, and the disseminated pyrite was cut by chalcopyrite + electrum veins
HJ-019kuaiPY@2	Stage II	Pyrite	1.7	
HJ-019kuaiPY@3	Stage II	Pyrite	1.8	
HJ-044-1PY@01	Stage III	Pyrite (Type B)	8.5	Disseminated Stage III pyrite coexists with chalcopyrite and pyrrhotite
HJ-044-1PY@2	Stage III	Pyrite (Type B)	10.0	
HJ-044-2PY@01	Stage III	Pyrite (Type B)	8.0	
HJ-044-2PY@2	Stage III	Pyrite (Type B)	8.2	
HJ-044-2PY@3	Stage III	Pyrite (Type B)	8.8	
HJ-044-1CCP@01	Stage III	Chalcopyrite	6.1	
HJ-044-2CCP@2	Stage III	Chalcopyrite	6.1	
HJ-044-2CCP@3	Stage III	Chalcopyrite	5.1	
HJ-064PY@01	Stage III	Pyrite (Type A)	−0.7	Disseminated pyrite and hematite cut host rock
HJ-064PY@2	Stage III	Pyrite (Type A)	3.7	
HJ-064PY@3	Stage III	Pyrite (Type A)	3.7	
HJ-064PY@4	Stage III	Pyrite (Type A)	4.3	
HJ-065-1PY@01	Stage III	Pyrite (Type A)	1.9	Pyrite vein cut tuffaceous host rock, and pyrite intergrows with minor hematite
HJ-065-1PY@2	Stage III	Pyrite (Type A)	2.4	
HJ-065-2PY@01	Stage III	Pyrite (Type A)	1.7	
HJ-065-2PY@2	Stage III	Pyrite (Type A)	1.5	
HJ-065-2PY@3	Stage III	Pyrite (Type A)	2.3	
HJ-090-1PY@01	Stage III	Pyrite (Type B)	4.6	Massive pyrite coexists with quartz in sulfide ore, and pyrite was cut by both Stage IV chalcopyrite veins and Stage V calcite
HJ-090-1PY@2	Stage III	Pyrite (Type B)	4.6	
HJ-090-1PY@3	Stage III	Pyrite (Type B)	4.8	
HJ-090-1PY@4	Stage III	Pyrite (Type B)	5.0	
HJ-090-2PY@01	Stage III	Pyrite (Type B)	5.1	
HJ-090-2PY@2	Stage III	Pyrite (Type B)	6.1	
HJ-090-2PY@3	Stage III	Pyrite (Type B)	5.4	
HJ-092PY@01	Stage III	Pyrite (Type A)	3.8	Disseminated pyrite in epidote altered host rock
HJ-092PY@2	Stage III	Pyrite (Type A)	2.6	
HJ-019kuaiCCP@01	Stage IV	Chalcopyrite	−1.5	Disseminated Stage II pyrite cut by Stage IV chalcopyrite + electrum veins
HJ-019kuaiCCP@2	Stage IV	Chalcopyrite	−3.5	
HJ-019-1CCP@01	Stage IV	Chalcopyrite	−1.1	Disseminated Stage IV chalcopyrite ± electrum veins replaced massive magnetite ore
HJ-019-1CCP@2	Stage IV	Chalcopyrite	−3.1	
HJ-019-1CCP@3	Stage IV	Chalcopyrite	−1.4	
HJ-019-1CCP@4	*Stage IV*	*Chalcopyrite*	*−5.7*	
HJ-019-1CCP@5	*Stage IV*	*Chalcopyrite*	*−7.1*	
HJ-019-2CCP@01	Stage IV	Chalcopyrite	−1.0	
HJ-019-2CCP@2	Stage IV	Chalcopyrite	−1.0	
HJ-019-2CCP@3	Stage IV	Chalcopyrite	−0.9	
HJ-019-2CCP@4	Stage IV	Chalcopyrite	−1.2	
HJ-019-2CCP@5	Stage IV	Chalcopyrite	−1.0	
HJ-019-2CCP@6	Stage IV	Chalcopyrite	−1.2	
HJ-019-2CCP@7	Stage IV	Chalcopyrite	−1.1	

Samples shown in italics were not used in the discussion.

Table 6
Summary of sulfur isotopic composition of minerals and ore-forming fluids in the Heijianshan Fe–Cu (–Au) deposit.

Stage	Magnetite mineralization (Stage II)	Pyrite alteration (Stage III)		Cu (-Au) mineralization (Stage IV)
$\delta^{34}S_{V\text{-}CDT}$ (‰)	+1.7‰ to +4.3‰	Type A: −0.7‰ to +4.3‰	Type B: +4.6‰ to +10.0‰	−3.5‰ to −0.9‰
Estimated temperature	~590 °C	119–262 °C (peak at 170 °C)		170–290 °C (average to 240 °C)
	Magnetite–actinolite oxygen isotope geothermometer	Fluid inclusions		Chlorite thermometer
fO_2 indicator	Magnetite	Hematite	Pyrrhotite	Chalcopyrite
$\Delta = \delta^{34}S_{H2S} - \delta^{34}S_{fluid}$	0‰	−25.0‰	0‰	−5.0‰
$\delta^{34}S_{fluid}$ (‰)	+1.7‰ to +4.3‰	+24.3‰ to +29.3‰	+4.6‰ to +10.0‰	+1.5‰ to +4.1‰

These values are distinctly higher than those with a typical magmatic–hydrothermal source ($\delta^{34}S = 0 \pm 5‰$; Ohmoto and Goldhaber, 1997), but lower than Late Carboniferous basinal brines (constrained by coeval seawater: ~13–19‰, Holser, 1977; Fig. 13b). This was probably resulted from the interactions between basinal brines and volcanic/volcaniclastic host rocks of the Matoutan Formation under low fO_2 (constrained by pyrrhotite buffer) condition. In Stage III, only minor chalcopyrite was precipitated with Type B pyrite. In Stage IV, $\delta^{34}S_{fluid}$ values of the ore-forming fluids (1.5–4.1‰) are generally similar to those from magmatic reservoirs ($\delta^{34}S = 0 \pm 5‰$; Ohmoto and Goldhaber, 1997) and lower than those of Stage III (Fig. 12), indicative of a magmatic–hydrothermal origin. However, the low temperatures (chlorite geothermometer: < 250 °C) and mineral paragenesis of the Stage IV fluids suggest that a magmatic–hydrothermal source was unlikely. An alternative interpretation for that would be the continuous and intensive interactions between basinal brines and the andesitic host rocks, which leached sulfur and Cu from the latter, yielding Cu-rich ore-forming fluids and the magmatic–hydrothermal sulfur isotope signatures.

As formerly discussed, the sulfur sources in the Heijianshan deposit may have changed from magmatic–hydrothermal (Stage II), through basinal brine-related (Stage III) to basinal brine–andesitic host rock interactions (Stage IV). Iron for the magnetite mineralization was likely derived from the magmatic–hydrothermal fluids, and sulfur isotopes and

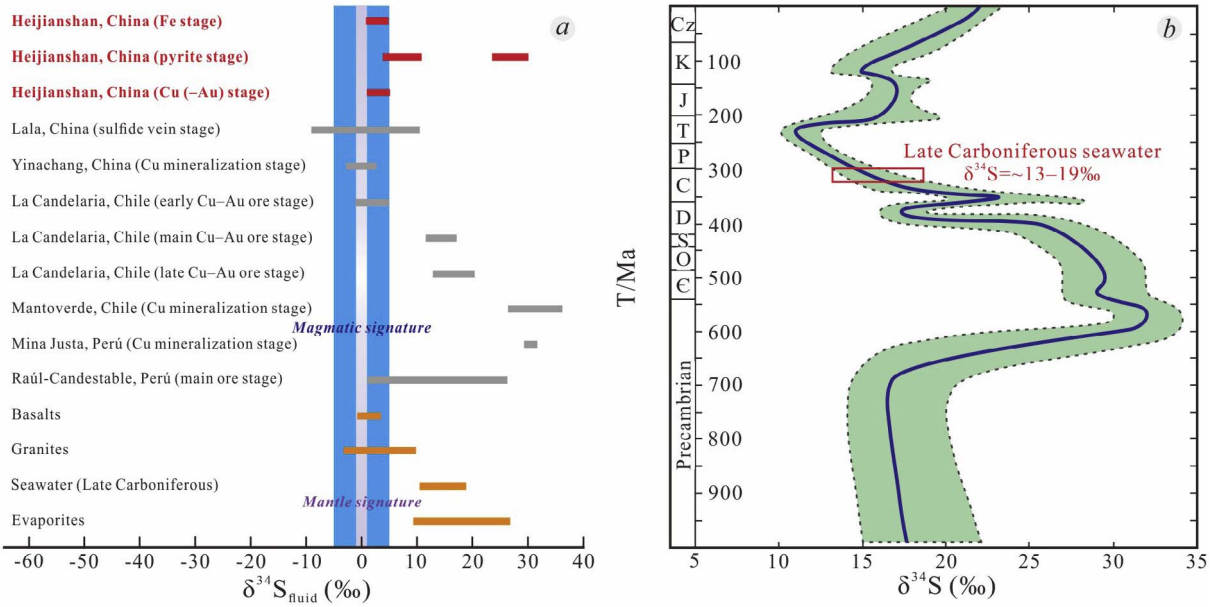

Fig. 13. (a). $\delta^{34}S_{fluid}$ values of ore-forming fluids at Heijianshan and other major IOCG deposits (data from Hoefs, 1997; Ullrich and Clark, 1999; Ullrich et al., 2001; Benavides et al., 2007; De Haller and Fontboté, 2009; Chen et al., 2011; Chen and Zhou, 2012; Li et al., 2015). (b). Sulfur isotopic compositions of global seawater through geological time (modified after Holser, 1977).

replacement textures (between chalcopyrite and early magnetite–pyrite) suggest that the metals for the Cu (–Au) mineralization was probably leached from the andesitic host rocks of the Matoutan Formation.

7.2. Evolution of ore-forming fluids

7.2.1. Epidote alteration

At Heijianshan, Stage I fluid inclusion microthermometric data suggest that the fluids of the epidote alteration were 189–370 °C, Ca–Mg-rich with variable low–high salinities (Figs. 10 and 14; Table 4), indicative of seawater–host rock interactions. We propose that the extensive epidote alteration at Heijianshan deposit may have formed from the reaction of the Late Carboniferous seawater (residues from the intra-/back-arc basin closure led by the S-dipping Kangguer oceanic slab subduction; Zhang et al., 2016) with volcanic/volcaniclastic host rocks, which was probably heated during the crystallization of chromite (residual mineral in the host rocks and replaced/cut by magnetite; Zhao et al., 2016) and cooling of the mafic magma (Zhao et al., 2017b; Fig. 15a).

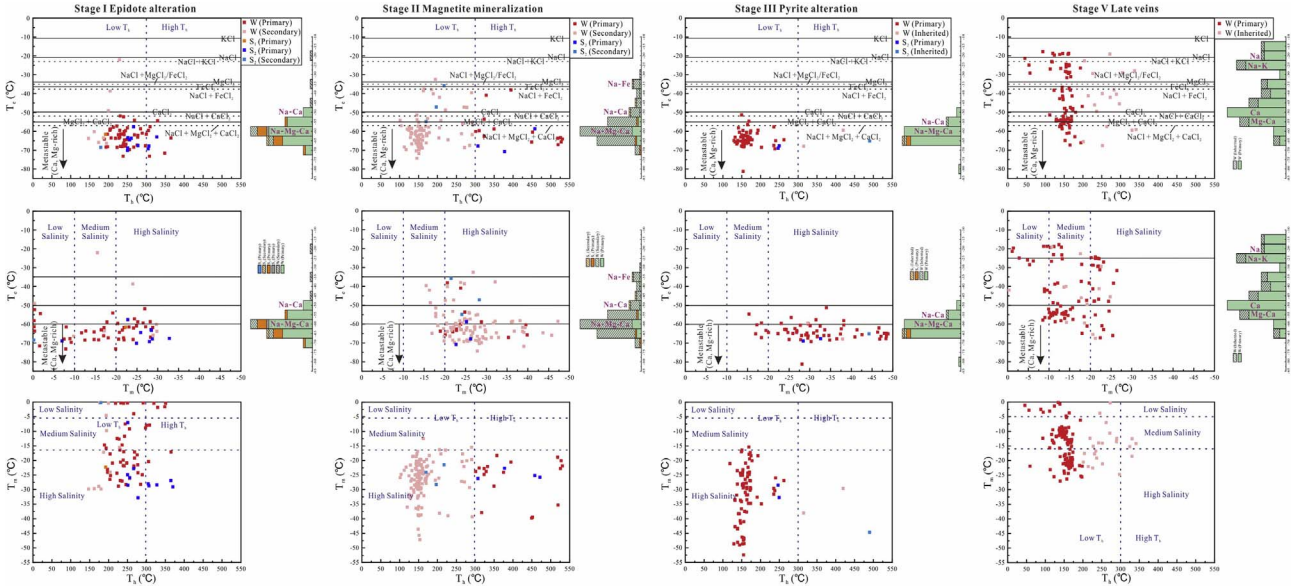

Fig. 14. Relationships among T_e, T_m and T_h for fluid inclusions of the Heijianshan epidote alteration, magnetite mineralization, pyrite alteration and late veins stages. The eutectic temperatures of systems with different components are indicated. The observed T_e ranges of the systems of NaCl–$CaCl_2$–H_2O (Samson et al., 2003), $CaCl_2$–H_2O (Lu et al., 2004), NaCl–$MgCl_2$–H_2O (Dubois and Marignac, 1997) and NaCl–$MgCl_2$–$CaCl_2$–H_2O (Chen et al., 2011) are shown in T_e vs. T_h space. Low and high temperature populations are divided at 300 °C on the basis of T_h. Low-, medium- and high-salinity inclusions are differentiated on the basis of T_m (0 °C to −10 °C, −10 °C to −20 °C and less than −20 °C, respectively). The histograms of the populations, with inferred dominant cations (see discussion part), are shown on the right. Different eutectic temperatures of systems with different components are from Lu et al. ((2004); KCl–H_2O, NaCl–H_2O, $FeCl_2$–H_2O, $MgCl_2$–H_2O, $FeCl_3$–H_2O), Samson et al. ((2003); NaCl–KCl-H_2O), Borisenko ((1977); NaCl–$FeCl_2$–H_2O) and Chen et al. ((2011); $MgCl_2$–$CaCl_2$–H_2O).

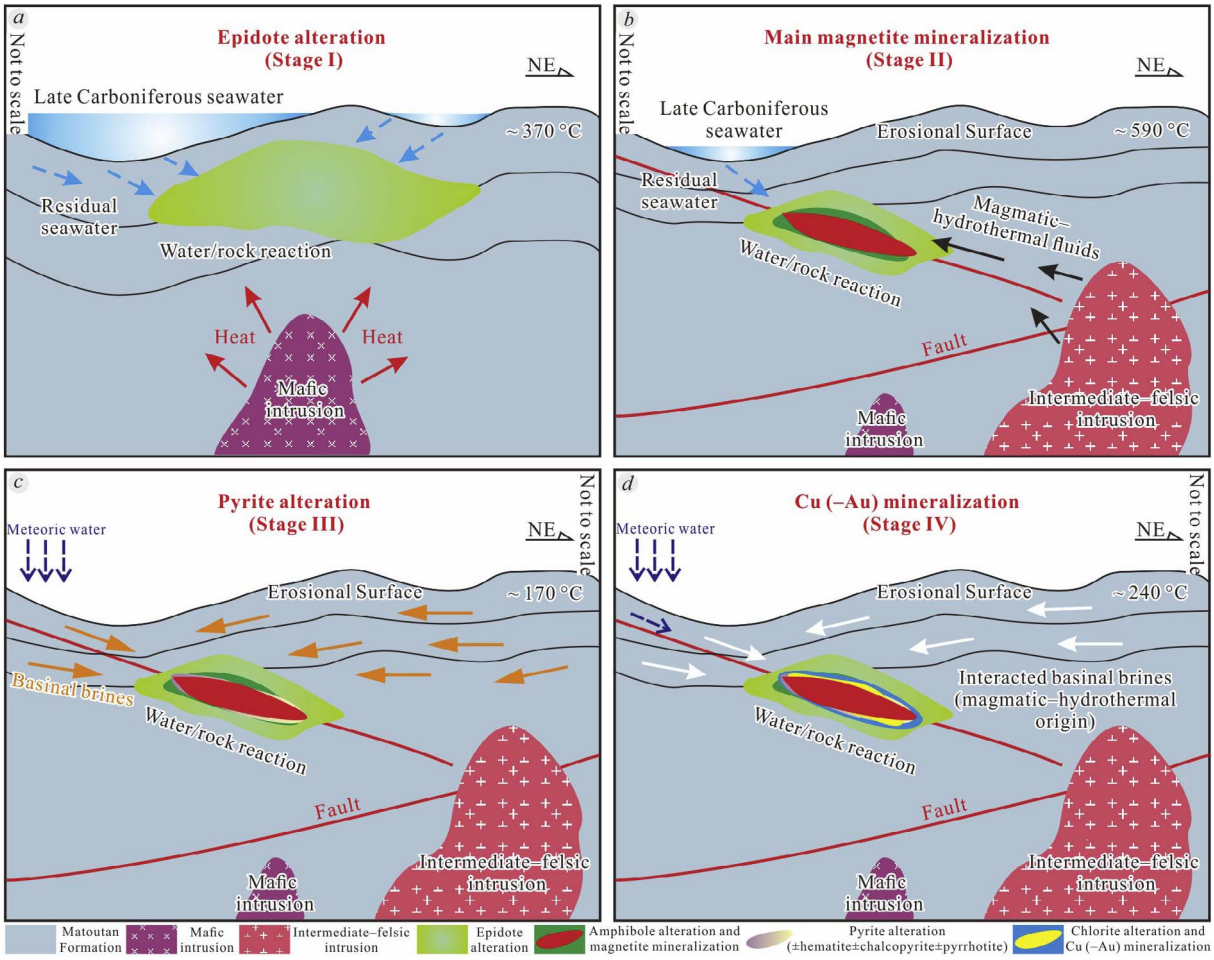

Fig. 15. Schematic diagrams illustrating the evolution of the Heijianshan deposit.

7.2.2. Iron mineralization

Both the T_h (301–536 °C) of the Stage II-B primary fluid inclusions (Table 4) and magnetite–actinolite oxygen isotope geothermometic result (~590 °C; Zhao et al., 2017b) indicate high Fe mineralization temperatures. The low T_m values (−39.8 °C to −18.3 °C; modes at −35 °C and −25 °C) of these primary inclusions suggest medium–high salinities (Fig. 10; Table 4), whilst the low T_e values (−70.8 °C to −38.1 °C; mode mainly at −60 °C) indicate Na–Ca–Mg–Fe-dominated fluids (Figs. 10 and 14), as also supported by the Stage II mineral assemblage of amphibole + sphene + apatite + magnetite. Besides, anhydrite- or hematite-bearing S-type fluid inclusions (Fig. 8g, h and k) also suggest that the fluids were Ca- and Fe-rich, respectively, and with relatively high fO_2. The high temperature mineral assemblage and sulfur isotopes (average 2.6‰) all indicate a magmatic–hydrothermal source for the Stage II ore-forming fluids, yet the Ca–Mg-rich nature and relatively light H isotope (Zhao et al., 2017b) may suggest possible limited residual seawater involvement. The Stage II ore-forming fluids were Fe-rich and oxidized (hematite buffer), as shown by the hematite precipitation at the beginning of this stage. The ascent of Stage II fluids along faults and the accompanied water/rock reactions may have lowered the fO_2 and precipitated magnetite (and also amphibole + quartz + K-feldspar) ores including massive, disseminations, clasts and veins, comprising the Heijianshan magnetite orebodies (Fig. 15b).

7.2.3. Pyrite alteration and Cu (–Au) mineralization

Primary fluid inclusions in Stage III quartz contain much lower T_h values (119–262 °C; peak at 170 °C) than those of the Stage II fluids (Fig. 10; Table 4), and show medium–high salinities and Na–Ca–Mg-rich features (Fig. 14). These features may indicate dominance of seawater or basinal brines for the Stage III fluids, and more likely the latter source which is supported by the extremely high $\delta^{34}S_{fluid}$ values (Fig. 13a). The transition of fluid sources from seawater (in Stage I) to basinal brines (in Stage III) may have occurred during basin closure and continuous evaporation. During late Stage III, the basinal brines may have started to leach limited amount of sulfur and copper from the andesitic host rocks to form the pyrite alteration (with decreasing fO_2, as shown by the transition from the hematite to pyrite–pyrrhotite buffer; Fig. 15c). The continuous tectonic compression and basin inversion may have further promoted the leaching process, yielding more Cu and Au and forming the Stage IV chalcopyrite (quartz + chlorite ± electrum ± hematite) in Cu (–Au) ore veins at ~240 °C (constrained by the chlorite geothermometer; Table 1; Fig. 15d).

7.2.4. Late hydrothermal veining

In Stage V, the low temperature (~160 °C) fluids consisted of two groups (Figs. 10 and 14), *viz.*, Ca–Mg-dominant with medium–high salinities (T_m < −10 °C) and Na–K-rich with low salinities ($T_m \geq -10$ °C). The former may have evolved from Stage III (pyrite alteration) fluids with a basinal brine origin, whereas the latter may have had a meteoric water-dominated origin. The changes of fluid sources from magmatic–hydrothermal (in Stage II) to meteoric water (in Stage V) are also recorded in H–O isotopes (Zhao et al., 2017b), and the Stage V alteration generated late-hydrothermal veins that crosscut the earlier-stage hydrothermal/mineralization minerals.

Table 7
Comparison between the Heijianshan Fe–Cu (–Au) deposit in the Eastern Tianshan and typical IOCG deposits in the Central Andes.

Deposits	Heijianshan, China	Mina Justa, Perú	Raúl-Condestable, Perú	Mantoverde, Chile	La Candelaria, Chile
Tectonic setting	basin inversion	basin inversion (basin-arc transformation)	basin inversion (basin-arc transformation)	basin inversion (basin-arc transformation)	basin inversion (basin-arc transformation)
Host rocks	tuff, brecciated tuff	andesite, andesitic volcaniclastic rock	tuff, agglomerate, greywacke, andesitic lava, pyroclastic rock, siltstone, limestone	andesitic lava, volcaniclastic rock	volcanic and volcaniclastic rock
Alteration[a]	(1) Ca–Mg (epidote and sericite) alteration; (2) amphibole + K-feldspar alteration with magnetite mineralization; (3) chlorite alteration with Cu (–Au) mineralization	(1) Na and K–Fe (albite, actinolite, microcline and magnetite) alteration; (2) actinolite (–magnetite) alteration; (3) potassic alteration with magnetite–pyrite mineralization; (4) Cu mineralization with calcite–hematite	(1) biotite alteration; (2) magnetite–actinolite/chlorite–sericite alteration; (3) Cu mineralization with/without magnetite and hematite	(1) albite alteration; (2) K-feldspar alteration with magnetite mineralization; (3) chlorite–sericite–scapolite–pyrite alteration; (4) Cu mineralization with hematite-calcite	(1) Na alteration; (2) biotite–magnetite alteration; (3) main-stage Cu mineralization with magnetite–amphibole alteration (Ca alteration) and hematite–calcite
Mineral assemblages[b,c]	mag–am–*qtz* + kfs *qtz*–ccp–chl + elc + hem	mag–py–*qtz*–chl ccp–bn–*cal*–hem–cc	act–scp–qtz–hem–mag ccp–py–po–*qtz* ± mag	mag–kfs + bt ccp–hem–*cal*–*qtz* + Au	hem–mag–kfs–bt–qtz ccp–hem–cal–chl + Au
Temperature[b] (°C)	~590 ~240	540–600 88–220 (140[d])	380–414 320–360 (350)	460–550 150–360 (240)	500–600 early: 400–450; middle: 300–400; late: 200–300
Salinity[b,e]	medium–high /	/ 6–32 (24)	/ > 20	3.4–63.9 14–40	high high
Fluid composition[b]	Na–Ca–Mg–Fe Ca–Mg	Na? Ca	/ Na (Ca?)	Ca Na (Ca?)	/ Na (Ca)
$\delta^{18}O_{fluid}$[b] (‰)	8.8–9.7 /	9.5–11.5 0.1	9.1–12.6 8.0–12.0	7.9–9.9 6.3–7.9	7.0–10.0 early: 8.0; middle: 5.0–8.0; late: 0.2–4.0
$\delta^{34}S_{fluid}$[b] (‰)	1.7–4.3 1.5–4.1	0.8–3.9 ≥29.3	/ 1.0–26.3	0.4–4.0 26.4–36.2	/ early: 1.0–5.7; middle: 9.0–13.0; late: 12.0–20.2
Fluid source[b]	Magmatic–hydrothermal (magma) Magmatic–hydrothermal (volcanic strata)	Magmatic–hydrothermal basinal brines	Magmatic–hydrothermal seawater	Magmatic–hydrothermal seawater	Magmatic–hydrothermal basinal brines or seawater
Age[b] (Ma)	< 315.6 ± 2.6 (zircon U–Pb) /	101–104 (microcline Ar–Ar) 95–99 (microcline Ar–Ar)	115.2 ± 0.3 (sphene U–Pb) /	116 (magnetite Re–Os) /	114.2 ± 0.8 (biotite Ar–Ar) 111.7 ± 0.8 (biotite Ar–Ar)
References	This study;Zhao et al. (2017a)	Chen et al. (2010, 2011)	Ripley and Ohmoto (1979), De Haller et al. (2006), De Haller and Fontboté (2009)	Mathur et al. (2002), Benavides et al. (2007), Rieger et al. (2012)	Ullrich and Clark (1999), Marschik and Fontboté (2001), Ullrich et al. (2001)

act, actinolite; *am*, amphibole; *bn*, bornite; *bt*, biotite; *cal*, calcite; *cc*, chalcocite; *ccp*, chalcopyrite; *chl*, chlorite; *elc*, electrum; *hem*, hematite; *kfs*, K-feldspar; *mag*, magnetite; *po*, pyrrhotite; *py*, pyrite; *qtz*, quartz; *scp*, scapolite.

[a] Numbers indicate the approximate paragenetic sequence.

[b] The first line for Fe mineralization, while the second line for Cu (–Au) mineralization.

[c] Italicized mineral used for fluid inclusion study.

[d] The majority.

[e] Weight percent NaCl equiv. or weight percent NaCl + $CaCl_2$ equiv.

7.3. Ore genesis

The Heijianshan Fe–Cu (–Au) deposit is hosted in the volcanic/volcaniclastic sequences and was regarded to be volcanic (Han et al., 2002; Pan et al., 2005; Liu, 2008; Wang et al., 2008), sedimentary deformation (Cui et al., 2008) or volcanic sedimentary (Zhang, 2000) deposit. Recently, some researchers proposed the Heijianshan as a skarn deposit (Mao et al., 2005; Pirajno, 2013) because of regionally developed intrusions (the Bailingshan intrusive complex) in the Aqishan-Yamansu belt. These genetic types for the Heijianshan Fe–Cu (–Au) deposit are controversial and many of them are not acceptable in worldwide recognized genetic classification.

Although the Heijianshan Fe–Cu (–Au) deposit shares many similarities in terms of host rocks and alteration styles with other Fe (–Cu) deposits in the Aqishan-Yamansu belt (e.g., Hongyuntan, Bailingshan and Yamansu), its distinct Fe mineralization mineral assemblages (magnetite and amphibole with no garnet or pyroxene) and the lack of clear relationships between orebodies and ore-related intrusions are different from typical skarn deposits (Meinert, 1992; Meinert et al., 2005). Furthermore, magnetite commonly intergrows with epidote after the prograde skarn (garnet and pyroxene) stage in typical Fe (–Cu) skarn deposits (Zhu et al., 2015), whereas at Heijianshan the epidote alteration clearly predated the magnetite mineralization (Figs. 5 and 6d). This also indicates that the Heijianshan is not a typical skarn deposit.

The Heijianshan Fe–Cu (–Au) deposit shares similar tectonic setting and certain alteration/mineralization features with some IOCG deposits in the Mesozoic Central Andean IOCG belt, e.g., Mina Justa and Raúl-Candestable (Perú), Mantoverde and La Candelaria (Chile) (Table 7). The epidote alteration stage at Heijianshan contains a Ca–Mg alteration assemblage of epidote–calcite–tourmaline–sericite, comparable to the widely developed pre-mineralization Na–Ca alteration in the Central Andes (Williams et al., 2005; Chen, 2013), and the alteration style differences (Na, Ca or Na–Ca) may have been attributed to the different types of host rocks (Zhao et al., 2017b). Iron and Cu (–Au) mineralization at Heijianshan are associated with amphibole + K-feldspar and chlorite + hematite alterations, respectively, also comparable with the Central Andean IOCG deposits, especially in the quartz/calcite–chalcopyrite–hematite assemblage for the Cu (–Au) mineralization (Table 7). Ore-forming fluids for the Fe and Cu (–Au) mineralization are high temperature, medium–high salinity and Na–Ca–Mg–Fe-dominated, and low temperature and Ca–Mg-dominated, respectively. Their oxygen and sulfur isotopes show similar magmatic–hydrothermal affinities but with different contribution of magma and volcanic rocks for Fe and Cu (–Au) mineralization, respectively (Table 7).

The Heijianshan Fe–Cu (–Au) deposit is mainly hosted by tuff and brecciated tuff of the Carboniferous Matoutan Formation (315.6 ± 2.6 Ma; Zhao et al., 2017a), suggesting that the Heijianshan Fe–Cu (–Au) mineralization likely occurred after 316 Ma. Recently, Zhang et al. (2016) proposed that the Aqishan-Yamansu belt was a back-/intra-arc basin (~350–325 Ma) formed by the S-dipping subduction of the Kangguer oceanic slab beneath the Yili-Central Tianshan block. The gradual closure of the Kangguer Ocean may have generated the widespread arc-related magmatism and the Aqishan-Yamansu basin inversion (~325–300 Ma), resulting in the Heijianshan Fe and Cu (–Au) mineralization. The close association of basin inversion with regional IOCG mineralization (~120–100 Ma) was also recorded in the Central Andes (Chen et al., 2013). These many similarities suggest that the Heijianshan is probably a Paleozoic IOCG-like deposit.

In the NW China, many Fe (–Cu) deposits are distributed, such as in the Eastern Tianshan. These deposits are mostly submarine volcanic-hosted and were thus classified as submarine volcanic-hosted deposits or submarine volcanogenic iron oxide (SVIO) deposits (Hou et al., 2014; Z.C. Zhang et al., 2014). These Fe (–Cu) deposits, especially those developed in arc/arc-basin belts of the Eastern Tianshan, Western Tianshan and Altay, may have formed during the later complex arc-basin transformation movements triggered by arc-arc or arc-continental collisions. This may have generated the regional submarine volcanic-hosted Fe and Cu (–Au) mineralization in those submarine volcanic-hosted Fe–Cu deposits, similar to the Heijianshan deposit in the Aqishan-Yamansu belt of the Eastern Tianshan. Those Fe–Cu deposits developed in arc-basin tectonic settings with obvious distinct Fe and Cu mineralization may provide suggestions to prospect copper and/or gold resources or even IOCG deposits in northern Xinjiang.

8. Conclusions

Alteration/mineralization of the Heijianshan Fe–Cu (–Au) deposit consisted of six stages, namely epidote alteration, magnetite mineralization, pyrite alteration, Cu (–Au) mineralization, late veins and supergene alteration. From the Fe mineralization to Cu (–Au) mineralization, the medium–high salinity ore-forming fluids were marked by significant decrease in Fe concentrations and temperatures (from ~590 °C to < 300 °C). The continuous S-dipping subduction of the Kangguer oceanic slab and basin inversion in the Aqishan-Yamansu belt have led to the leaching of volcanic/volcaniclastic rocks of the Late Carboniferous Matoutan Formation by external basinal brines, generating firstly pyrite alteration and then Cu (–Au) mineralization. The Heijianshan Fe–Cu (–Au) deposit shares many similarities with the Mesozoic Central Andean IOCG deposits in terms of alteration, mineral paragenesis, tectonic setting, as well as mineralization fluid and its source, which suggests that the Heijianshan is probably a Paleozoic IOCG-like deposit, and implies exploration potential for IOCG or IOCG-like deposits in the Aqishan-Yamansu belt of the Eastern Tianshan, NW China.

Acknowledgments

This study was financially supported by the Chinese National Basic Research 973-Program (2014CB440802), Strategic Priority Research Program (B) of the Chinese Academy of Sciences (XDB1800000), CAS-SAFEA International Partnership Program for Creative Research Teams (20140491534) and SKL-ODG Open Funds (201508). We thank Drs. Bing Xiao and Pin Wang from the Guangzhou Institute of Geochemistry, Chinese Academy of Sciences for their help in the EPMA and SEM-CL analyses. We are also grateful to the Xinjiang No. 1 Geological Team for their field assistance, and Drs. Jinsheng Han, Chengming Wang and Jing Fang from the Guangzhou Institute of Geochemistry, Chinese Academy of Sciences, for their help in the preparation and discussion of this paper. Anonymous reviewers and the editor (Franco Pirajno) have provided insightful comments for an earlier version of the manuscript. This is contribution No. IS-2439 from GIGCAS.

Appendix A. Supplementary data

Supplementary data associated with this article can be found, in the online version, at http://dx.doi.org/10.1016/j.oregeorev.2017.10.014.

References

Allan, M.M., Yardley, B.W., 2007. Tracking meteoric infiltration into a magmatic–hydrothermal system: a cathodoluminescence, oxygen isotope and trace element study of quartz from Mt. Leyshon, Australia. Chem. Geol. 240, 343–360.
Benavides, J., Kyser, T., Clark, A.H., Oates, C.J., Zamora, R., Tarnovschi, R., Castillo, B., 2007. The Mantoverde iron oxide–copper–gold district, III Región, Chile: The role of regionally derived, nonmagmatic fluids in chalcopyrite mineralization. Econ. Geol. 102, 415–440.
Bodnar, R.J., 1993. Revised equation and table for determining the freezing point depression of H2O–NaCl solutions. Geochim. Cosmochim. Acta 57, 683–684.
Borisenko, A.S., 1977. Study of the salt composition of solutions in gas–liquid inclusions in minerals by the cryometric method. Sov. Geol. Geophys. 18, 11–18.
Charvet, J., Shu, L.S., Charvet, S.L., 2007. Paleozoic structural and geodynamic evolution of eastern Tianshan (NW China): welding of the Tarim and Junggar plates. Episodes 30, 162–186.
Chen, H.Y., 2013. External sulfur in IOCG mineralization: implications on definition and

classification of the IOCG clan. Ore Geol. Rev. 51, 74–78.
Chen, W.T., Zhou, M.F., 2012. Paragenesis, stable isotopes, and molybdenite Re–Os isotope age of the Lala iron-copper deposit, Southwest China. Econ. Geol. 107, 459–480.
Chen, H.Y., Clark, A.H., Kyser, T.K., Ullrich, T.D., Baxter, R., Chen, Y.M., Moody, T.C., 2010. Evolution of the giant Marcona-Mina Justa iron oxide–copper–gold district, south-central Peru. Econ. Geol. 105, 155–185.
Chen, H.Y., Kyser, T.K., Clark, A.H., 2011. Contrasting fluids and reservoirs in the contiguous Marcona and Mina Justa iron oxide–Cu (–Ag–Au) deposits, south-central Perú. Miner. Deposita 46, 677–706.
Chen, Y.J., Pirajno, F., Wu, G., Qi, J.P., Xiong, X.L., 2012. Epithermal deposits in north Xinjiang, NW China. Int. J. Earth Sci. 101, 889–917.
Chen, H.Y., Cooke, D.R., Baker, M., 2013. Mesozoic iron oxide copper–gold mineralization in the central Andes and the Gondwana Supercontinent breakup. Econ. Geol. 108, 37–44.
Cheng, S.L., Wang, X.K., Wu, H., Mao, Q.G., Ao, S.J., Han, C.M., 2008. Late Paleozoic endogenic metallogenic series in the North Mountains, Xinjiang, NW China. Xinjiang Geol. 26, 43–48 (in Chinese with English abstract).
Cui, B., He, Z.J., Zhao, L., Dong, L.H., Liu, T., Qu, J., 2008. Research on metallogenic systems of gold and copper deposits in the middle section of Eastern Tianshan, Xinjiang, China. Earth Sci. Front. 15, 13–17 (in Chinese with English abstract).
De Haller, A., Fontboté, L., 2009. The Raúl-Condestable iron oxide copper-gold deposit, central coast of Peru: ore and related hydrothermal alteration, sulfur isotopes, and thermodynamic constraints. Econ. Geol. 104, 365–384.
De Haller, A., Corfu, F., Fontboté, L., Schaltegger, U., Barra, F., Chiaradia, M., Frank, M., Alvarado, J.Z., 2006. Geology, geochronology, and Hf and Pb isotope data of the Raúl-Condestable iron oxide–copper–gold deposit, central coast of Peru. Econ. Geol. 101, 281–310.
Deng, X.H., Wang, J.B., Wang, Y.W., Li, Y.C., Fang, T.H., Mao, Q.G., 2014. Geological characteristics of the Hongshi Cu–Au deposit, Eastern Tianshan, Xinjiang and discussion of the deposit genesis. Miner. Explor. 5, 159–168 (in Chinese with English abstract).
Dubois, M., Marignac, C., 1997. The H_2O–NaCl–$MgCl_2$ ternary phase diagram with special application to fluid inclusion studies. Econ. Geol. 92, 114–119.
Eldridge, C.S., Compston, W., Williams, I.S., Harris, J.W., Bristow, J.W., 1991. Isotope evidence for the involvement of recycled sediments in diamond formation. Nature 353, 649–653.
Evans, K.A., Tomkins, A.G., Cliff, J., Fiorentini, M.L., 2014. Insights into subduction zone sulfur recycling from isotopic analysis of eclogite-hosted sulfides. Chem. Geol. 365, 1–19.
Gao, J., Li, M.S., Xiao, X.C., Tang, Y.Q., He, G.Q., 1998. Paleozoic tectonic evolution of the Tianshan Orogen, northwestern China. Tectonophysics 287, 213–231.
Goldstein, R.H., 2003. Petrographic analyses of fluid inclusions. In: Samson, I., Anderson, A., Marshall, D. (eds.), Fluid inclusion-analysis and interpretation. Mineralogical Association of Canada Short Course Series 32, pp. 9–54.
Goldstein, R.H., Reynolds, T.J., 1994. Systematics of fluid inclusions in diagenetic minerals. Soc. Sedim. Geol.SEPM Short Course 31.
Han, C.M., Mao, J.W., Yang, J.M., Wang, Z.L., Cui, B., 2002. Research on metallogenic series of copper-polymetallic deposits in East Tianshan Mountains. Miner. Deposita 21, 125–127 (in Chinese).
Han, B.F., Guo, Z.J., Zhang, Z.C., Zhang, L., Chen, J.F., Song, B., 2009. Age, geochemistry, and tectonic implications of a late Paleozoic stitching pluton in the North Tian Shan suture zone, western China. Geol. Soc. Am. Bull. 122, 627–640.
Han, C.M., Xiao, W.J., Zhao, G.C., Su, B.X., Sakyi, P.A., Ao, S.J., Wan, B., Zhang, J., Zhang, Z.Y., 2014. Late Paleozoic metallogenesis and evolution of the East Tianshan Orogenic Belt (NW China, Central Asia Orogenic Belt). Geol. Ore Deposits 56, 493–512.
He, Z.Y., Klemd, R., Zhang, Z.M., Zong, K.Q., Sun, L.X., Tian, Z.L., Huang, B.T., 2015. Mesoproterozoic continental arc magmatism and crustal growth in the eastern Central Tianshan Arc Terrane of the southern Central Asian Orogenic Belt: geochronological and geochemical evidence. Lithos 236, 74–89.
Hoefs, J., 1997. Stable isotope geochemistry. Berlin, pp. 1–285.
Holser, W.T., 1977. Catastrophic chemical events in history of the ocean. Nature 267, 402–408.
Hou, T., Zhang, Z.C., Pirajno, F., Santosh, M., Encarnacion, J., Liu, J.L., Zhao, Z.D., Zhang, L.J., 2014. Geology, tectonic settings and iron ore metallogenesis associated with submarine volcanism in China: an overview. Ore Geol. Rev. 57, 498–517.
Huang, X.W., Zhou, M.F., Qi, L., Gao, J.F., Wang, Y.W., 2013a. Re–Os isotopic ages of pyrite and chemical composition of magnetite from the Cihai magmatic–hydrothermal Fe deposit, NW China. Miner. Deposita 48, 925–946.
Huang, X.W., Qi, L., Meng, Y.M., 2013b. Trace element and REE geochemistry of minerals from Heifengshan, Shuangfengshan and Shaquanzi (Cu–) Fe deposit, eastern Tianshan Mountains. Miner. Deposita 32, 1188–1210 (in Chinese with English abstract).
Huang, X.W., Qi, L., Gao, J.F., Zhou, M.F., 2013c. First reliable Re–Os ages of pyrite and stable isotope compositions of Fe (–Cu) deposits in the Hami Region, Eastern Tianshan Orogenic Belt, NW China. Resour. Geol. 63, 166–187.
Huang, B.T., He, Z.Y., Zhang, Z.M., Klemd, R., Zong, K.Q., Zhao, Z.D., 2015a. Early Neoproterozoic granitic gneisses in the Chinese Eastern Tianshan: petrogenesis and tectonic implications. J. Asian Earth Sci. 113, 339–352.
Huang, Z.Y., Long, X.P., Kröner, A., Yuan, C., Wang, Y.J., Chen, B., Zhang, Y.Y., 2015b. Neoproterozoic granitic gneisses in the Chinese Central Tianshan Block: implications for tectonic affinity and Precambrian crustal evolution. Precambr. Res. 269, 73–89.
Jahn, B.M., Wu, F.Y., Chen, B., 2000. Massive granitoid generation in Central Asia: Nd isotope evidence and implication for continental growth in the Phanerozoic. Episodes 23, 82–92.
Jahn, B.M., Windley, B., Natal'in, B., Dobretsov, N., 2004. Phanerozoic continental growth in Central Asia. J. Asian Earth Sci. 23, 599–603.
Jiang, F.Z., Qin, K.Z., Fang, T.H., Wang, S.L., 2002. Types, geological characteristics, metallogenic regularity and exploration target of iron deposits in Eastern Tianshan Mountains. Xinjiang Geol. 20, 379–383 (in Chinese with English abstract).
Jiang, H.J., Han, J.S., Chen, H.Y., Zheng, Y., Zhang, W.F., Lu, W.J., Deng, G., Tan, Z.X., 2016. Hydrothermal alteration, fluid inclusions and stable isotope characteristics of the Shaquanzi Fe-Cu deposit, Eastern Tianshan: implications for deposit type and metallogenesis. Ore Geol. Rev. http://dx.doi.org/10.1016/j.oregeorev.2016.09.025.
Kita, N.T., Ushikubo, T., Fu, B., Valley, J.W., 2009. High precision SIMS oxygen isotope analysis and the effect of sample topography. Chem. Geol. 264, 43–57.
Kranidiotis, P., Maclean, W.H., 1987. Systematics of chlorite alteration at the Phelpa Dodge massive sulfide deposit, Mategami, Quebec. Econ. Geol. 82, 1898–1911.
Leake, B.E., Woolley, A.R., Hawthorne, F.C., Kato, A., Kisch, H.J., Krivovivhev, V.G., Linthout, K., Laird, J., Maresch, W.V., Schumacher, J.C., Stephenson, N.C.N., Whittaker, E.J.W., Guo, Y.Z., 1997. Nomenclature of amphiboles: Report of the subcommittee on amphiboles of the international mineralogical association, commission on new minerals and mineral names. Can. Miner. 35, 219–246.
Lei, R.X., Wc, C.Z., Gu, L.X., Zhang, Z.Z., Chi, G.X., Jiang, Y.H., 2011. Zircon U-Pb chronology and Hf isotope of the Xingxingxia granodiorite from the Central Tianshan zone (NW China): implications for the tectonic evolution of the southern Altaids. Gondwana Res. 20, 582–893.
Lei, R.X., Wu, C.Z., Zhang, Z.Z., Gu, L.X., Tang, J.H., Li, G.R., 2013. Geochronology, geochemistry and tectonic significances of the Yamansubei pluton in eastern Tianshan, Northwest China. Acta Pet. Sin. 29, 2653–2664 (in Chinese with English abstract).
Li, X.J., Li, X.H., 1999. Geology and metallogenesis of the Bailingshan iron deposit in Shanshan, Xinjiang. Geol. Prospect. 35, 9–13 (in Chinese with English abstract).
Li, Y., Yang, J.S., Zhang, J., Li, T.F., Chen, S.Y., Ren, Y.F., Xu, X.Z., 2011. Tectonic significance of the Carboniferous volcanic rocks in eastern Tianshan. Acta Pet. Sin. 27, 193–209 (in Chinese with English abstract).
Li, H.M., Ding, J.H., Li, L.X., Yao, T., 2014. The genesis of the skarn and the genetic type of the Yamansu iron deposit, Eastern Tianshan, Xinjiang. Acta Geol. Sin. 88, 2477–2489 (in Chinese with English abstract).
Li, X.C., Zhao, X.F., Zhou, M.F., Chen, W.T., Chu, Z.Y., 2015. Fluid inclusion and isotopic constraints on the origin of the Paleoproterozoic Yinachang Fe-Cu-(REE) deposit, Southwest China. Econ. Geol. 110, 1339–1369.
Li, D.F., Zhang, L., Chen, H.Y., Hollings, P., Cao, M.J., Fang, J., Wang, C.M., Lu, W.J., 2016. Geochronology and geochemistry of the high Mg dioritic dikes in Eastern Tianshan, NW China: geochemical features, petrogenesis and tectonic implications. J. Asian Earth Sci. 115, 442–454.
Liu, W., 2008. Geological characteristics and prospecting direction of copper deposits in the Eastern Tianshan, Xinjiang. Xinjiang Youse Jinshu 31, 30–32 (in Chinese).
Liu, S.W., Guo, Z.J., Zhang, Z.C., Li, Q.G., Zheng, H.F., 2004. Nature of the Precambrian metamorphic blocks in the eastern segment of Central Tianshan: Constraints from geochronology and Nd isotopic geochemistry. Sci. China, Ser. D Earth Sci. 47, 1085–1094.
Lu, H.Z., Fan, H.R., Ni, P., Ou, G.X., Shen, K., Zhang, W.H., 2004. Fluid inclusions. Science Press, Beijing, pp. 1–487 (in Chinese).
Ma, Q., Chen, G., 2011. Major types and geological characteristics of copper deposits in the Eastern Tianshan. West-China Explor. Eng. 23, 201–202 (in Chinese).
Mao, J.W., Goldfarb, R.J., Wang, Y.T., Hart, C.J., Wang, Z.L., Yang, J.M., 2005. Late Paleozoic base and precious metal deposits, East Tianshan, Xinjiang, China: characteristics and geodynamic setting. Episodes 28, 23–30.
Marschik, R., Fontboté, L., 2001. The Candelaria-Punta del Cobre iron–oxide Cu–Au (–Zn–Ag) deposits, Chile. Econ. Geol. 96, 1799–1826.
Mathur, R., Marschik, R., Ruiz, J., Munizaga, F., Leveille, R.A., Martin, W., 2002. Age of mineralization of the Candelaria iron oxide Cu–Au deposit, and the origin of the Chilean Iron Belt based on Re–Os isotopes. Econ. Geol. 97, 59–71.
Meinert, L.D., 1992. Skarns and skarn deposits. Geosci. Can. 19, 145–162.
Meinert, L.D., Dipple, G.M., Nicolescu, S., 2005. World skarn deposits. Economic Geology 100th Anniversary Volume pp. 299–336.
Monteiro, L.V.S., Xavier, R.P., Hitzman, M.W., Juliani, C., Filho, C.R.D.S., Carvalho, E.D.R., 2008. Mineral chemistry of ore and hydrothermal alteration at the Sossego iron oxide–copper–gold deposit, Carajás Mineral Province, Brazil. Ore Geol. Rev. 34, 317–336.
Ohmoto, H., Goldhaber, M.B., 1997. Sulfur and carbon isotopes. In: Barnes, H.L. (Ed.), Geochemistry of Hydrothermal Ore Deposits. Wiley, New York, pp. 517–612.
Ohmoto, H., Rye, R.O., 1979. Isotopes of sulfur and carbon. In: Barnes, H.L. (Ed.), Geochemistry of Hydrothermal Ore Deposits. Wiley, New York, pp. 509–567.
Oyman, T., 2010. Geochemistry, mineralogy and genesis of the Ayazmant Fe–Cu skarn deposit in Ayvalik (Balikesir), Turkey. Ore Geol. Rev. 37, 175–201.
Pan, C.Z., Xiao, W.J., Cui, B., Han, C.M., 2005. Geological characteristics of copper deposits in the middle section of the East Tianshan Mountains. Xinjiang Geol. 23, 127–130 (in Chinese with English abstract).
Pirajno, F., 2013. The geology and tectonic settings of China's mineral deposits. Springer Sci. Bus. Media 1–679.
Qin, K.Z., Xiao, W.J., Zhang, L.C., Xu, X.W., Hao, J., Sun, S., Li, J.L., Tosdal, R.M., 2005. Eight Stages of Major Ore Deposits in Northern Xinjiang, NW-China: Clues and Constraints on the Tectonic Evolution and Continental Growth of Central Asia// Mineral Deposit Research: Meeting the Global Challenge. Springer, Berlin Heidelberg, pp. 1327–1330.
Redmond, P.B., Einaudi, M.T., Inan, E.E., Landtwing, M.R., Heinrich, C.A., 2004. Copper deposition by fluid cooling in intrusion-centered systems: new insights from the Bingham porphyry ore deposit, Utah. Geology 32, 217–220.
Rieger, A.A., Marschik, R., Díaz, M., 2012. The evolution of the hydrothermal IOCG system in the Mantoverde district, northern Chile: new evidence from

microthermometry and stable isotope geochemistry. Miner. Deposita 47, 359–369.
Ripley, E.M., Ohmoto, H., 1979. Oxygen and hydrogen isotopic studies of ore deposition and metamorphism at the Raul mine, Peru. Geochim. Cosmochim. Acta 43, 1633–1643.
Roedder, E., Ribbe, P., 1984. Fluid inclusions. Rev. Mineral. 12, 644–645.
Rusk, B., Reed, M., 2002. Scanning electron microscope-cathodoluminescence analyses of quartz reveals complex growth histories in veins from the Butte porphyry copper deposit, Montana. Geology 30, 727–730.
Rusk, B.G., Lowers, H.A., Reed, M.H., 2008. Trace elements in hydrothermal quartz: relationships to cathodoluminescent textures and insights into vein formation. Geology 36, 547–550.
Samson, I., Anderson, A., Marshall, D.D., 2003. Fluid inclusions: Analyses and interpretation. Mineralogical Association of Canada.
Sengör, A.M.C., Natal'in, B.A., 1996. Paleotectonics of Asia: fragments of synthesis. In: Yin, A., Harrison, T.M. (Eds.), The Tectonic Evolution of Asia. Cambridge University Press, Cambridge, pp. 486–640.
Ullrich, T.D., Clark, A.H., 1999. The Candelaria Cu–Au deposit, III Región, Chile: paragenesis, geochronology and fluid composition. In: Stanley, C.J. (Ed.), Mineral Deposits: Processes to Processing. Balkema, Rotterdam, pp. 201–204.
Ullrich, T.D., Clark, A.H., Kyser, T.K., 2001. The Candelaria Cu–Au deposit, III Región, Chile: Product of long-term mixing of magmatic–hydrothermal and evaporite-sourced fluids. GSA Annual Meeting, Boston, Abstracts with Programs, A-3.
Wang, J.B., Wang, Y.W., He, Z.J., 2006. Ore deposits as a guide to the tectonic evolution in the East Tianshan Mountains, NW China. Chin. Geol. 33, 461–469 (in Chinese with English abstract).
Wang, X.K., Deng, J., Wu, H., Chen, S.L., Deng, G., Ao, S.J., Chai, F.M., 2008. Geological characteristics of major endogenetic metal deposits in the Weiquan-Caixiashan section of the East Tianshan Mountains, NW China. Chin. Geol. 26, 17–21 (in Chinese with English abstract).
Wang, M., Zhang, J.J., Zhang, B., Qi, G.W., 2015. An Early Paleozoic collisional event along the northern margin of the Central Tianshan Block: constraints from geochemistry and geochronology of granitic rocks. J. Asian Earth Sci. 113, 325–338.
Wilkinson, J., Boyce, A., Earls, G., Fallick, A., 1999. Gold remobilization by low-temperature brines; evidence from the Curraghinalt gold deposit, Northern Ireland. Econ. Geol. 94, 289–296.
Williams, P.J., Barton, M.D., Johnson, D.A., Fontboté, L., Halter, A.D., Mark, G., Oliver, N.H.S., Marschik, R., 2005. Iron oxide copper–gold deposits: Geology, space-time distribution, and possible modes of origin. Econ. Geol. 371–405.
Windley, B.F., Alexeiev, D., Xiao, W.J., Kröner, A., Badarch, G., 2007. Tectonic models for accretion of the Central Asian Orogenic Belt. J. Geol. Soc. 164, 31–47.
Wu, C., Chen, H.Y., Liang, P., Han, J.S., Liu, Z.J., Fang, J., Xu, D.R., 2016. Paragenesis and fluid evolution of the Halasu III porphyry Cu deposit, East Junggar (NW China): Implications for the Paleozoic multiphase superimposing mineralization in the Central Asian Orogenic Belt. Ore Geol. Rev. doi: 10.1016/j.oregeorev.2016.08.001.
Xiao, W.J., Zhang, L.C., Qin, K.Z., Sun, S., Li, J.L., 2004. Paleozoic accretionary and collisional tectonics of the Eastern Tianshan (China): implications for the continental growth of central Asia. Am. J. Sci. 304, 370–395.
Xiao, W.J., Han, C.M., Yuan, C., Sun, M., Lin, S.F., Chen, H.L., Li, Z.L., Li, J.L., Sun, S., 2008. Middle Cambrian to Permian subduction-related accretionary orogenesis of Northern Xinjiang, NW China: implications for the tectonic evolution of central Asia. J. Asian Earth Sci. 32, 102–117.
Xiao, W.J., Windley, B.F., Huang, B.C., Han, C.M., Yuan, C., Chen, H.L., Sun, M., Sun, S., Li, J.L., 2009. End-Permian to mid-Triassic termination of the accretionary processes of the southern Altaids: implications for the geodynamic evolution, Phanerozoic continental growth, and metallogeny of Central Asia. Int. J. Earth Sci. 98, 1189–1217.
Xiu, Q.Y., Fei, Y.H., Quan, L., 2002. A single zircon U-Pb age for the granodiorite of Kawabulake complex, Xinjiang, China. Xinjiang Geol. 20, 335–337 (in Chinese with English abstract).
Xu, S.Q., Zhao, T.Y., Feng, J., Gao, Y.F., Tian, J.T., Yang, Z.F., Liu, D.Q., 2011. Study on regional metallogenic regularity of marine volcanic type iron ore in the East Tianshan of Xinjiang. Xinjiang Geol. 29, 173–177 (in Chinese with English abstract).
Xu, L.L., Chai, F.M., Li, Q., Zeng, H., Geng, X.X., Xia, F., Deng, G., 2014. Geochemistry and zircon U-Pb age of volcanic rocks from the Shaquanzi Fe–Cu deposit in East Tianshan Mountains and their geological significance. Chin. Geol. 41, 1771–1790 (in Chinese with English abstract).
Xinjiang Uygur Autonomous Region Geological Survey (abv. XUARGS), 2003. Report for target selection and potential resources in Caixiashan-Jintan in the Eastern Tianshan, Xinjiang, pp. 1–187 (in Chinese).
Zeng, H., Chai, F.M., Zhou, G., Geng, X.X., Li, Q., Meng, Q.P., Xu, L.L., 2014. Mineralogy of skarn and magnetite of the Yamansu iron deposit and its geological significance. Chin. Geol. 41, 1914–1928 (in Chinese with English abstract).
Zhang, H.Y., 2000. Geological features and genesis classification of the iron belt in the south of Shanshan, Xinjiang. Northwestern Geol. 33, 15–18 (in Chinese).
Zhang, D.Y., 2012. Petrogenesis, mineralization and geodynamic evolution in Jueluotage area, Eastern Tianshan, Northwest China. Ph.D thesis, Hefei, China, Hefei University of Technology, pp. 1–217 (in Chinese with English abstract).
Zhang, D.Y., Zhou, T.F., Yuan, F., Liu, S., Lu, Y.J., Xu, C., Ning, F.Q., 2012. Geochronology and geological indication of the native copper mineralized basalt formation in Jueluotage area, Eastern Tianshan, Xinjiang. Acta Pet. Sin. 28, 2392–2400 (in Chinese with English abstract).
Zhang, Z.J., Sun, J.B., Hu, M.Y., Ji, H.W., Chen, W., 2012. Study on stable isotopic characteristics of the Hongyuntan iron deposit of Eastern Tianshan and their implications for the process of mineralization. Acta Geosci. Sin. 33, 918–924 (in Chinese with English abstract).
Zhang, L.C., Wang, Y.T., Chen, X.F., Ma, S.Q., Wang, Z.H., Yu, C.F., 2013. Mineralogy, mineral chemistry and genesis of the Hongyuntan iron deposit in East Tianshan Mountains, Xinjiang. Acta Pet. Miner. 32, 431–449 (in Chinese with English abstract).
Zhang, D.Y., Zhou, T.F., Yuan, F., Fan, Y., Deng, Y.F., Xu, C., Zhang, R.F., 2014. Genesis of Permian granites along the Kangguer Shear Zone, Jueluotage area, Northwest China: geological and geochemical evidence. Lithos 198, 141–152.
Zhang, L., Chen, H.Y., Zheng, Y., Qin, Y.J., Li, D.F., 2014. Geology, fluid inclusion and age constraints on the genesis of the Sarekuobu gold deposit in Altay, NW China. Geol. J. 49, 635–648.
Zhang, W.F., Chen, H.Y., Zhao, L.D., 2014. Alteration and mineralization paragenesis of the Bailingshan Fe (–Cu) deposit in Eastern Tianshan. Acta Geol. Sin. (English Edition) 88, 405–406.
Zhang, Z.C., Hou, T., Santosh, M., Li, H.M., Li, J.W., Zhang, Z.H., Song, X.Y., Wang, M., 2014. Spatio-temporal distribution and tectonic settings of the major iron deposits in China: an overview. Ore Geol. Rev. 57, 247–263.
Zhang, W.F., Chen, H.Y., Han, J.S., Zhao, L.D., Huang, J.H., Yang, J.T., Yan, X.L., 2016. Geochronology and geochemistry of igneous rocks in the Bailingshan area: implications for the tectonic setting of Late Paleozoic magmatism and iron skarn mineralization in the eastern Tianshan, NW China. Gondwana Res. 38, 40–59.
Zhao, L.D., Chen, H.Y., Zhang, L., Li, D.F., Zhang, W.F., Wang, C.M., Yang, J.T., Yan, X.L., 2016. Magnetite geochemistry of the Heijianshan Fe-Cu (-Au) deposit in Eastern Tianshan: metallogenic implications for submarine volcanic-hosted Fe-Cu deposits in NW China. Ore Geol. Rev. http://dx.doi.org/10.1016/j.oregeorev.2016.07.022.
Zhao, L.D., Chen, H.Y., Zhang, L., Zhang, W.F., Yang, J.T., Yan, X.L., 2017a. The Late Paleozoic magmatic evolution of the Aqishan-Yamansu belt, Eastern Tianshan: constraints from geochronology, geochemistry and Sr–Nd–Pb–Hf isotopes of igneous rocks. J. Asian Earth Sci. http://dx.doi.org/10.1016/j.jseaes.2017.07.038.
Zhao, L.D., Chen, H.Y., Zhang, L., Zhang, Z.J., Li, D.F., Zhang, W.F., Lu, W.J., Yang, J.T., Yan, X.L., 2017b. H-O isotope characteristics and geological significance of the Heijianshan Fe–Cu (–Au) deposit in the Eastern Tianshan, Xinjiang. Miner. Deposits 36, 38–56 (in Chinese with English abstract).
Zhou, T.F., Yuan, F., Zhang, D.Y., Fan, Y., Liu, S., Peng, M.X., Zhang, J.D., 2010. Geochronology, tectonic setting and mineralization of granitoids in Jueluotage area, eastern Tianshan, Xingjiang. Acta Pet. Sin. 26, 478–520 (in Chinese with English abstract).
Zhu, Q.Q., Xie, G.Q., Mao, J.W., Li, W., Li, Y.H., Wang, J., Zhang, P., 2015. Mineralogical and sulfur isotopic evidence for the incursion of evaporites in the Jinshandian skarn Fe deposit, Edong district, Eastern China. J. Asian Earth Sci. 113, 1253–1267.